

# Modelling and Control of MPPT Converters for DC Microgrids

Thesis Report  
by  
Neil Dani



DELFT UNIVERSITY OF TECHNOLOGY

MASTER THESIS

ET4300

---

# Modelling and Control of MPPT Converters for DC Microgrids

---

*Neil Dani*

(5274826)

MSc Electrical Engineering

Track: Electrical Power Engineering

---

*Authors:*

Neil Dani 5274826

*Committee Members:*

Prof. Arno Smets

Dr. Laura Ramirez Elizondo

Dr. Patrizio Manganiello

Dr. Laurens Mackay

Gerasimos Maroulis

August 18, 2022



To tackle the effect of climate change while meeting the ever-growing demand of energy, a high scale of integration of renewable energy resources has been performed in the past decade. Solar Photovoltaics have played a monumental role in this process, thus contributing in the fulfillment of the energy demand. The scalability and the flexibility of use has led to a significant development in the technologies implemented for assimilation of Solar PV. In addition, the development in power electronics has made the process of integration seamless. Due to Solar PV's dependency on irradiation there is an ever growing need for establishment of an improved control on power converters.

The aim of this thesis is to implement Maximum Power Point Tracking and Droop control algorithms on PV powered DC-DC Converters while considering the dynamics of Solar PV. Mathematical modelling is used to model the PV generator to consider its dynamics along with the dynamics of the converters to establish control. The output of these converters is connected to a DC Microgrid. After completion of the modelling process, the internal control design was performed followed by the implementation of both the algorithms. The project was performed at the lab of the company DC-Opportunities.

The findings of this research are presented in the current document. Its goal is to outline the procedure taken from the start of the project and the literature review all the way through the design and testing of the power electronic converters. Finally, suggestions for the future are offered, which might serve as a roadmap for more advancements.

---

## Acknowledgements

---

This thesis project is the last step in completing my studies in Electrical Power Engineering degree at Technical University of Delft. The goal of this thesis was something I was interested in.

During this process, I came across different obstacles concerning to the research as well as some my personal life. Nonetheless, I would like to thank those people who have stood by me all the way. Their support, encouragement and guidance has helped me during my time of education at TU Delft.

I would like to thank Dr. Patrizio Manganiello for the academic support he has offered me through out this thesis project. Additionally, Gerasimos Maroulis and Dr. Laurens Mackay deserve my gratitude. They both deserve my sincere appreciation for their perseverance, help, and the hours spent in conversation regarding my inquiries.

Finally I would like to thank my parents and friends for all the support during my time at TU Delft.

Abstract . . . . .	i
Acknowledgements . . . . .	ii
Acronyms . . . . .	v
List of Figures . . . . .	vi
List of Tables . . . . .	viii
<b>1 Introduction</b>	<b>1</b>
1.1 Problem Definition and Motivation . . . . .	1
1.2 Objective of the thesis . . . . .	4
1.3 Research Questions . . . . .	4
1.4 Overview of the thesis . . . . .	4
<b>2 Literature Review</b>	<b>6</b>
2.1 Mathematical Modelling . . . . .	6
2.2 State Space Modelling . . . . .	7
2.3 PV string Modelling based on the information in datasheet . . . . .	9
2.4 Modern PV based systems . . . . .	13
2.5 DC Microgrids, DC-DC Converters and Control . . . . .	14
2.5.1 Control of DC-DC Converters . . . . .	15
<b>3 State Space Modelling of MPPT converters</b>	<b>19</b>
3.1 Boost Converter for the tram lines . . . . .	19
3.1.1 Application in the project . . . . .	22
3.2 MPPT Converter for a Bipolar DC Micorgrid . . . . .	24
3.2.1 Application in the project . . . . .	27
3.3 Implementation of Control . . . . .	27
3.3.1 Boost Converter for tram lines . . . . .	28
3.3.2 MPPT Converter for a Bipolar DC Micorgrid . . . . .	31
3.4 C-Script and State Machine . . . . .	32
<b>4 Simulations and Hardware Testing</b>	<b>34</b>
4.1 Boost Converter for tram lines . . . . .	34
4.1.1 Simulation Results . . . . .	34
4.1.2 Hardware Results . . . . .	38
4.2 MPPT Boost Converter for Bipolar DC Microgrids . . . . .	44
4.2.1 Hardware Results . . . . .	44

<b>5</b>	<b>Conclusion and Further Development</b>	<b>49</b>
5.1	Conclusion . . . . .	49
5.1.1	Discussion on the research questions . . . . .	49
5.2	Further Developments . . . . .	49

---

## Acronyms

---

Abbreviation	Description
AC	Alternating Current
CCM	Continuous Conduction Mode
DC	Direct Current
DER	Distributed Energy Resource
GHG	Green House Gases
HVDC	High Voltage DC
IEA	International Energy Agency
KCL	Kirchoff's Current Law
KVL	Kirchoff's Voltage Law
LTI	Linear Time Invariant
MCU	micro-Controller Unit
MIMO	Multiple Input Multiple Output
MPPT	Maximum Power Point Tracking
P&O	Perturb and Observe
PCB	Printed Circuit Board
PI	Proportional-Integral
PLECS	Piecewise Linear Electrical Circuit Simulation
PV	Photovoltaics
SISO	Single Input Single Output
STC	Standard Testing Conditions

---

## List of Figures

---

1.1	Reduction in PV Costs over the next three decades. [1]	1
1.2	Rise in GHG Emissions and Temperature over this century [3]	2
1.3	Prediction of energy generation by renewable sources by 2050 [3]	3
2.1	Block Diagram of State Space Equations	7
2.2	Single and Double Diode Models of a PV Panel	9
2.3	I-V Curve of a PV Panel	10
2.4	P-V Curve of a PV Panel	10
2.5	Diode in the model of the PV generator	12
2.6	Different types of PV systems [18]	13
2.7	Typical configuration of a DC Microgrid [20]	14
2.8	Flowchart of Perturb and Observe MPPT Algorithm	16
2.9	Flowchart of Incremental Conductance MPPT Algorithm	17
2.10	Droop Control	18
3.1	Grid connected Boost Converter with PV as the input	19
3.2	PV powered Boost Converter for tram lines with PV model at its input	20
3.3	Current-Voltage curves for different irradiance levels based on the model created for the LG410N2W-L5 panel	23
3.4	Power-Voltage curves for different irradiance levels based on the model created for the LG410N2W-L5 panel	23
3.5	PV Powered Boost Converter for Bipolar DC Microgrids [34]	25
3.6	Grid connected Boost Converter for Bipolar DC Microgrids with PV model at its input	26
3.7	Cascade PI Control for the PV powered grid connected Boost Converter	28
3.8	Closed loop Step Response of Equation 3.35	29
3.9	Closed loop Step Response of the Equation 3.40	30
3.10	Closed loop Step Response of Equation 3.44	31
3.11	Closed loop Step Response of Equation 3.49	32
3.12	State Machine function flowchart	33
4.1	Variation in Irradiance during the operation in MPPT	35
4.2	Input Voltage vs Set Point under MPPT Operation	35
4.3	Input current vs Set Point under MPPT Operation	36
4.4	Voltage measurements during MPPT and Droop mode switching	37
4.5	Current measurements during MPPT and Droop mode switching	37
4.6	Hardware of the Boost Converter	38
4.7	Source and Load side	39

4.8	Input Voltage of the Boost Converter Hardware during MPPT operation . . . . .	39
4.9	Output Voltage of the Boost Converter Hardware during MPPT operation . . . . .	40
4.10	Input Current of the Boost Converter Hardware during MPPT . . . . .	40
4.11	MPP Point tracking on the I-V and P-V Curves for hardware . . . . .	41
4.12	Input Voltage of the Boost Converter during MPPT to Droop switching . . . . .	41
4.13	Output Voltage of the Boost Converter during MPPT to Droop switching . . . . .	42
4.14	Input Current of the Boost Converter during MPPT to Droop switching . . . . .	43
4.15	Hardware of the MPPT Boost Converter for Bipolar DC Microgrids . . . . .	44
4.16	MPPT Control test on the Hardware of the negative side . . . . .	44
4.17	Change in input current resulted due to change in Irradiance . . . . .	45
4.18	MPPT to Droop control switching test . . . . .	45
4.19	Output and Neutral point voltages of the Bipolar . . . . .	46
4.20	MPPT Control test on the Hardware of the negative side . . . . .	46
4.21	Change in input current resulted due to change in Irradiance . . . . .	47
4.22	Output and Neutral point voltages of the Bipolar . . . . .	47

---

## List of Tables

---

3.1	LG N-2 series' LG410N2W-L5 panel . . . . .	22
3.2	Calculated PV Model parameters . . . . .	24
3.3	Specifications of the MPPT Boost Converter . . . . .	24
3.4	Specifications of the MPPT Converter for Bipolar DC Microgrid . . . . .	27
4.1	Variation in the input current depending on the variation in Irradiance . . . . .	36

## 1.1 Problem Definition and Motivation

Over the past years, the integration of renewable energy resources has increased in order to reduce the carbon emissions in the power sector while meeting the ever-growing demand of energy. The global power sector is going through a major change where maintaining and increasing the availability of low cost renewable energy is a major point of focus. Solar PV has been one of the major renewable energy resources which has been integrated into the power systems on a massive scale over the years. Continuous evolution of PV Technologies has led to an improvement in the performance. Currently, Solar PV is already the lowest cost source of energy in many markets, and by 2030 it aims to be the benchmark low-cost technology across many more markets [1].

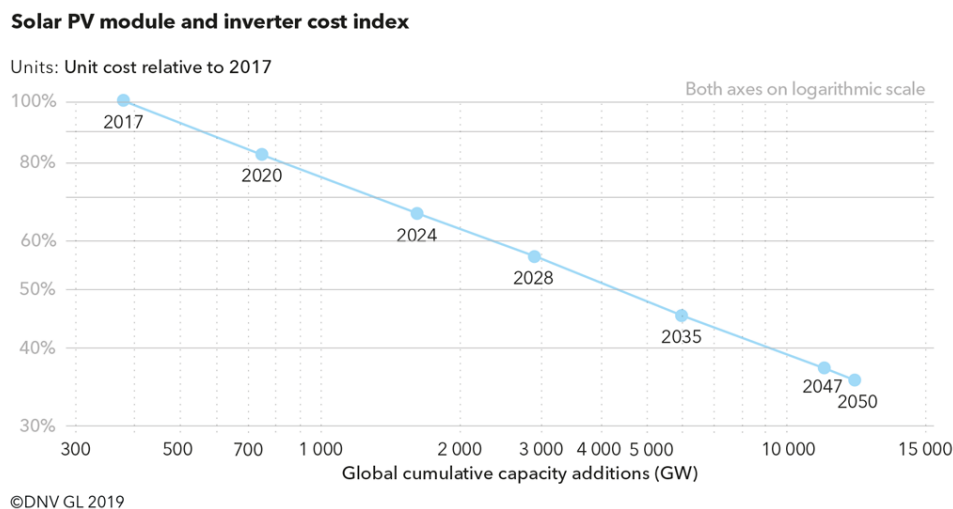


Figure 1.1: Reduction in PV Costs over the next three decades. [1]

The graph shown in figure 1.1 shows the decline in the cost of PV panels and inverters over the years. In 2017, Solar PV constituted 2% of the total energy provided in comparison to hydro electricity which was 15%. And, by 2030, Solar is expected to be at the same level as Hydro Electricity at 15%. With the growing energy demands, due to the growing population and their needs, the need to integrate renewable energy sources for electricity generation is more important [1]. According to [2] keeping the global temperature rise below 2 degrees Celsius ( $^{\circ}\text{C}$ ) is technically feasible, but the current emission trends are not on track. The world will run out of the energy related 'carbon budget' in the next

20 years if the domination of fossil fuels continues in the energy production. This indicates that use of Renewable Energy is very important in the energy transition process. And therefore, expansion of renewable energy's share should grow rapidly to meet the near-zero or net-zero CO<sub>2</sub> emissions. The IEA projects that despite the 4.4% drop in 2020 due to the COVID-19 pandemic and with the current policies in place, the GHG emissions will continue to rise before stabilizing around 2035. Temperatures would also increase in excess of 3°C (50% probability) above pre-industrial levels at the end of the century. The graph shown in figure 1.2 shows the rise in GHG emissions on the left and the temperature on the right side. [3]

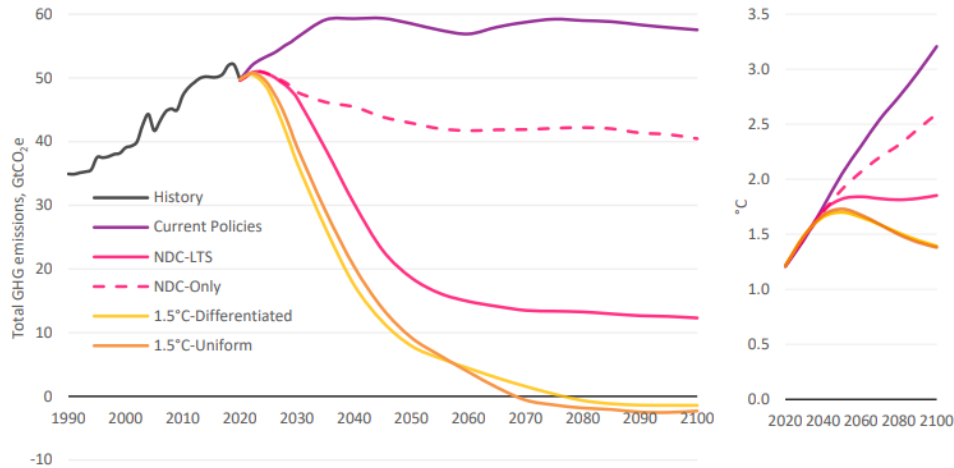


Figure 1.2: Rise in GHG Emissions and Temperature over this century [3]

In 2021, the Conferences of the Parties (COP26) took place where different countries submitted their Nationally Determined Contributions or NDCs. NDC is a climate action plan to cut emissions and adapt to climate impacts. On the basis of that, 'Global Energy and Climate Outlook 2021: Advancing towards climate neutrality', states that if the NDCs are met, then it would result into 1.8°C rise in mean global temperature. But, substantial actions still need to be taken to limit the rise in global mean temperature below the 2°C and pursue the target of 1.5°C above the pre-industrial levels. To make it possible, GECO2021 has modelled the 1.5°C-Uniform and 1.5°C-Differentiated scenarios. The 1.5°C-Uniform scenario is an economically efficient pathway to the 1.5°C climate target, as the uniform global carbon price ensures that emissions are reduced where abatement costs are lowest. The 1.5°C-Differentiated scenario carbon price is differentiated across regions according to their per-capita income, with richer regions having a higher carbon price and poorer regions progressively catching up to that price.

This initiative would boost the use of renewable energy resources thus eventually making them the primary source of power. Figure 1.3 shows that in 2050 energy produced by renewables will account for 78% of global power generation, mostly wind with a share of 31% and solar with a share of 25%. As a result of the increasing shares of these renewable technologies, the share of fossil fuel generation will reduce to 5% [3]. Over the past years, monumental progress has happened, when it comes to development and implementation of renewable energy powered technologies. The rise of solar farms, standalone solar PV powered facilities, the advent of electric vehicles, PV powered charging stations indicate that eventually, renewable energy could be the chief source of electricity. Such technological developments contribute to the generation of clean electricity. Most of these technologies like PV, produce DC and use DC-AC converters before feeding the power to the grid. Over the recent period in time, onshore and offshore PV farms have been expanding on the global level. All the power converters installed to extract their output operate on the Maximum Power Point Tracking (MPPT) algorithm, thus extracting the highest amount of power out of the PV generator installed, considering its intermittent nature. The DC output again requires DC-AC inverters for the AC grid connection.

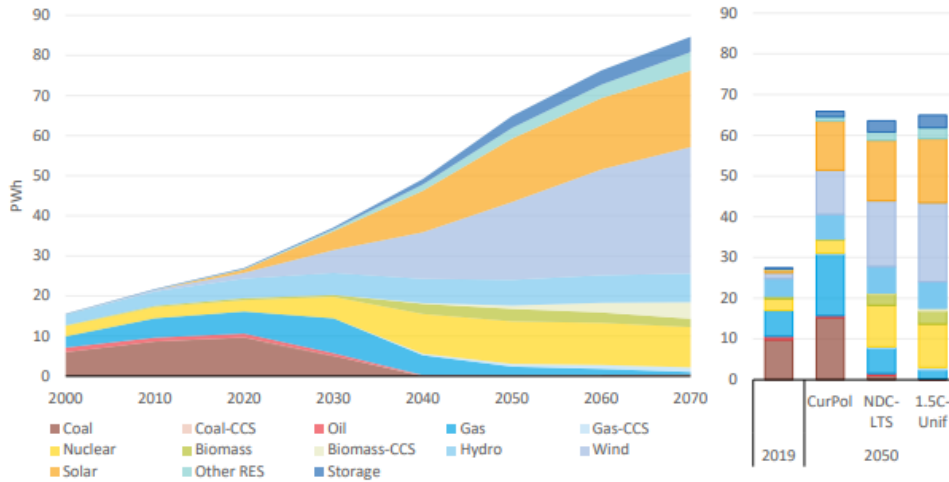


Figure 1.3: Prediction of energy generation by renewable sources by 2050 [3]

Solar PV is highly scalable and a non-obstructive resource of energy. It can be integrated with different objects giving rise to innovative applications like Building-integrated photovoltaics (BI-PV) and Vehicle-integrated photovoltaics (VI-PV). This results into heavy reduction in transmission losses. Along with this, many applications like LED lighting, consumer electronics like computers, cell-phones operate with DC, thus making DC to AC conversion an unnecessary step. All these factors result into a growing need for a DC grid. With the presence of DC grids, integration of PV and DC loads would be an easier process with lesser losses in the process [4]. Additionally, the modern power electronic semiconductors can handle significantly high voltage levels, in order to power many of the DC loads [5].

In all these applications DC-DC Converters play a vital role. They act as the interface between the source and the load where they step-up or step-down the input voltage depending on the requirement at the output. PV being an intermittent source of energy, provides a certain input at a specific time. Since most of the times the load requires constant voltage despite of the disturbances, establishment of control on the converters to avoid any instability is important. Public transport has been electrified over the years and integration of renewable energy resources has been a recent goal such that their dependency on coal fired power plants would reduce. Trains and trams are supplied by overhead power lines. By powering these modes of transport by renewable energy, the load on coal fired power plants can be reduced significantly. Such an implementation has been planned by HTM Personenvervoer, where they plan to use PV to power a section of their tram lines. Usually while designing the control for such applications, the intermittent characteristics, the dynamics of the PV generator under different operating conditions are not taken into account directly. As a result rudimentary control strategies are usually designed. Since PV generators have intermittent characteristics that may change the generated voltage depending on the irradiance and the operating temperature, MPPT control is implemented on the converter circuits. MPPT control helps in order to continuously track the point where maximum power can be obtained through the PV generator depending on the variations in operating conditions. Using this method, the dynamic factors of the source are taken into account resulting into a generation of highest amount of power for different operating conditions which include the variations in the irradiance of the sun and temperature. By considering the dynamics, the performance and the resilience of the control can be improved giving rise to a stable operation under all the operating conditions. Along with that, DC Microgrids are also an upcoming topic of research and implementation due to the advent of the Distributed Energy Resources (DERs) like PV. A microgrid is where most of the power required or all the power required is generated using renewable sources of energy independent of other sources of generation. A cluster of houses powered by PV only can be called as a microgrid. Microgrids are mostly located in remote areas where there is a lack of grid connection. A microgrid can function in islanded or grid connected mode. Droop control is usually

installed in order to make the islanding and de-islanding process successful. As a result, establishing control over microgrid connected converters which are powered by DERs has become an important area of research making this project vital.

## 1.2 Objective of the thesis

The main objective of this thesis is to establish control over DC Microgrid connected MPPT DC-DC Converters. Usually solar panels at the input of any DC-DC Converters are considered as a standard voltage source therefore not considering their dynamic characteristics with respect to generation of power. However, behaviour of Solar PV varies with respect to the different operating conditions and this results into an effect on the dynamic characteristics of the converter circuits as well. Therefore, a mathematical model of a PV string has been made and that has been combined with the converter's mathematical model. Followed by this, the next objective was to implement MPPT and Droop control on the converters in PLECS. Finally, after multiple simulations under different operating conditions, hardware implementation was carried out to validate the simulations.

## 1.3 Research Questions

In order to achieve the research objective, a set of research questions has been defined and will be answered in this thesis.

- **How does the PV model affect the control of the MPPT Converter?**

Usually, a PV string at the input is considered to be a regular voltage source to perform the analysis followed by the implementation of control on power converters. One of the goals of this thesis project was to make a mathematical model of a PV string to study its dynamics and how to consider those in controller design.

- **How can MPPT converters be operated in islanded and grid connected modes of operation?**

When multiple converters are connected in parallel to a DC Microgrid, the main aim is to maintain a uniform output voltage, which if not met, then results into circulating currents which results into a droop on the voltage. One of the goals of this thesis was to implement the droop control technique in order to tackle this problem.

## 1.4 Overview of the thesis

Throughout the course of this thesis research, relevant information was gathered from a variety of sources, including the fields of Control design, Photovoltaic based applications, and DC Microgrids. The content included in the research has been organized in different chapters and each one of them describes the details of the collected information. By following the report in an orderly manner, the reader can follow the development of the project starting from the problem definition to the testing results.

In Chapter 1 the adverse effects of climate change and the role renewable energy resources and power electronics have played in order to integrate the renewable energy resources have been discussed. Followed by that the research questions which formulate this thesis project have been discussed along with the structure.

Chapter 2 mainly focusses on the Literature review which includes concepts of Mathematical Modelling, information related to DC Microgrids and control algorithms for converters.

Chapter 3 deals with the State Space Modelling of MPPT DC-DC Converters for two distinct applications i.e. DC Microgrids and tramlines. The models of the converters have been explained followed by the design of the control loop for both. An insight about the State Machine implemented is also been given here.

Chapter 4 elaborates on the simulations and hardware testing experiments conducted on the converters to test the control loop. MPPT and Droop control was implemented and tested for operating modes.

In chapter 5, the summary of the results is been presented followed by the process of answering the research questions. Also, future recommendations are suggested here.

## 2.1 Mathematical Modelling

While studying Control Systems, we need to be able to model dynamic systems in mathematical terms and analyze their dynamic characteristics. We can represent the dynamic system by using a set of differential equations. We can obtain these differential equations using fundamental laws that govern a particular system (ie. Newton's Laws for Mechanical Systems, Kirchhoff's Laws for Electrical Systems, etc.). Obtaining and deriving these equations are the most important part of the entire analysis of control systems. The set of these derived equations result into the formation of a mathematical model. The experimental technique, also known as system identification, is to estimate the system using a mathematical model based on the outcomes of particular test input signals. The study of system identification has evolved into its own discipline. The theoretical analysis approach is mostly utilized in this section to build mathematical models of control systems. Mathematical Models may take many forms depending on the system. One modelling technique may be better suited than another for a specific type of system.

In this section, three different mathematical models discussed are Differential equation model, Transfer function model, and the State space model. Differential Equation Modelling follows the procedure for establishing the equations of a system or a component using the analytical method. The steps are to determine the system or component's inputs and outputs. Then to write the functions describing every part of the system in the sequence of the signal flow according to the Kirchhoff's laws. Followed by elimination of the intermediate variables to obtain the differential equations of the inputs and outputs. Lastly the equations are rewritten in the standard form by putting the input related terms. These equations are later solved to calculate their solutions. If the system is nonlinear then it is linearized based on reasonable rules to find approximate solutions since there is no universal solution for nonlinear differential equations.

The Transfer function model is an extended version of the Differential Equation model, but based on Laplace transform. Transfer function which is the ratio of the output to the input in Laplace domain, which helps in studying the dynamic response of the system, as well as the effect of the structure or the variations in the parameter. This approach considers the initial conditions to be zero. Along with that, this modelling technique only works for a SISO system [6].

The State Space Modelling approach is a time domain based approach that considers the initial conditions and is usable for MIMO systems. It can also be integrated with control strategies. Due to these advantages over the other modelling techniques, this modelling technique has been used to make the Mathematical Model of the DC-DC Converters. The next section elaborates on the steps of this modelling method.

## 2.2 State Space Modelling

The State Space model of a Linear Time-Invariant (LTI) system can be represented as follows.

$$\dot{x} = Ax + Bu \quad (2.1)$$

$$y = Cx + Du \quad (2.2)$$

Equation 2.1 is the State Equation and Equation 2.2 is the Output Equation.  $A, B, C, D$  are the State, Input, Output and Feed-forward matrices respectively.  $x$  is the state variable,  $\dot{x}$  is the state variable derivative,  $u$  is the input, and  $y$  is the output. The State Equation represents the rate of change of system state to the state variables and the input variables. And the Output Equation links the state and the input variables to the output variables. Figure 2.1 represents the structure and the formation

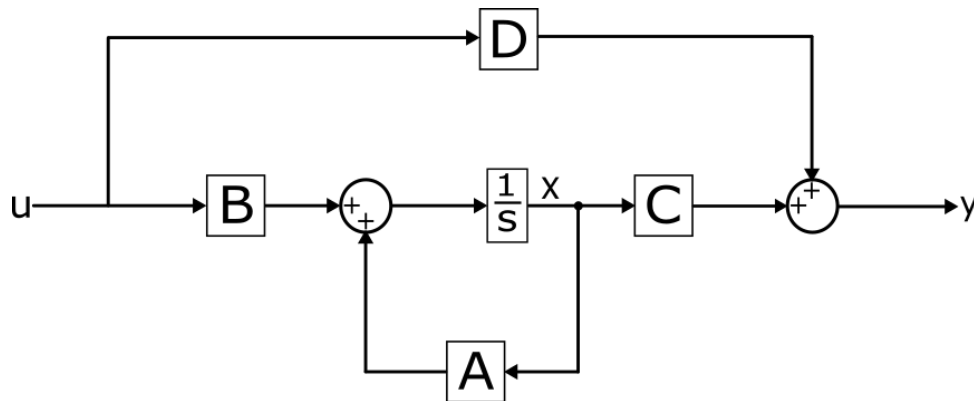


Figure 2.1: Block Diagram of State Space Equations

of the State Space Equations. The Electrical circuit is analysed using the Kirchoff's laws and the formed equations are written down in the format shown below. Later these equations are written in the Matrix format.  $A$  and  $C$  are square matrices of size  $m$ -by- $m$ , and matrices  $B$  and  $D$  are of size  $m$ -by- $n$  thus adequately representing equations 2.1 and 2.2. This set of equations has to be made for every switching state of the switching device used. Once that is done, then the equations are multiplied by on and off time duty cycles followed by their addition to get the averaged out equations. Thus while making a Mathematical model of the converter circuits, Kirchoff's laws are used to generate equations in the following form as shown below [7].

$$\begin{aligned} \dot{x}_1 &= a_{11}x_1 + a_{12}x_2 + \dots + a_{1n}x_n + b_{11}u_1 + b_{12}u_2 + \dots + b_{1m}u_m, \\ \dot{x}_2 &= a_{21}x_1 + a_{22}x_2 + \dots + a_{2n}x_n + b_{21}u_1 + b_{22}u_2 + \dots + b_{2m}u_m, \\ &\vdots \\ &\vdots \\ &\vdots \\ \dot{x}_n &= a_{n1}x_1 + a_{n2}x_2 + \dots + a_{nn}x_n + b_{n1}u_1 + b_{n2}u_2 + \dots + b_{nm}u_m \end{aligned}$$

After that is done, then the matrices are made as per the specific state and input parameters to result into the following form and accurately represents the equation  $\dot{x}=Ax+Bu$  where  $A$  is a square matrix of  $n \times n$  dimensions and  $B$  is a matrix of  $n \times m$  dimensions. Similarly,  $C$  and  $D$  matrices are made

resulting to represent  $y=Cx+Du$ .

$$\begin{pmatrix} \dot{x}_1 \\ \dot{x}_2 \\ \vdots \\ \dot{x}_n \end{pmatrix} = \begin{pmatrix} a_{11}a_{12}\dots a_{1n} \\ a_{21}a_{22}\dots a_{2n} \\ \vdots \\ a_{n1}a_{n2}\dots a_{nn} \end{pmatrix} \begin{pmatrix} x_1 \\ x_2 \\ \vdots \\ x_n \end{pmatrix} + \begin{pmatrix} b_{11}b_{12}\dots b_{1m} \\ b_{21}b_{22}\dots b_{2m} \\ \vdots \\ b_{n1}b_{n2}\dots b_{nm} \end{pmatrix} \begin{pmatrix} u_1 \\ u_2 \\ \vdots \\ u_m \end{pmatrix} \quad (2.3)$$

For an Electrical circuit, these equations are made for both the states i.e on-time (d) and off-time (1-d) thus giving a set of equations  $\dot{x} = A_1x + B_1u$  and  $y = C_1x + D_1u$  for on time and  $\dot{x} = A_2x + B_2u$  and  $y = C_2x + D_2u$  for off time. The matrices of each state are then multiplied with the respective duty cycles as shown below. Later they are added to get the averaged out matrices[7].

$$\begin{aligned} A_{avg} &= A_1 \cdot d + A_2 \cdot (1 - d) \\ B_{avg} &= B_1 \cdot d + B_2 \cdot (1 - d) \\ C_{avg} &= C_1 \cdot d + C_2 \cdot (1 - d) \\ D_{avg} &= D_1 \cdot d + D_2 \cdot (1 - d) \end{aligned} \quad (2.4)$$

Once the averaging part is complete, small signal perturbations are introduced i.e.  $x = X + \tilde{x}$ ,  $y = Y + \tilde{y}$ ,  $u = U + \tilde{u}$  and  $d = D + \tilde{d}$ . Here the block letters X,Y,U,D are steady state values and the terms  $\tilde{x}, \tilde{y}, \tilde{u}, \tilde{d}$  are the small signal perturbations[7]. Every state, input and output parameter and duty cycle is written in the manner shown above. After the perturbations are put and the terms are rearranged, equation 2.5 and 2.6 are obtained[8].

$$\dot{\tilde{x}} = A_{avg}X + B_{avg}U + A_{avg}\tilde{x} + B_{avg}\tilde{u} + [(A_1 - A_2)X + (B_1 - B_2)U]\tilde{d} + [(A_1 - A_2)\tilde{x} + (B_1 - B_2)\tilde{u}]\tilde{d} \quad (2.5)$$

$$Y + \tilde{y} = C_{avg}X + D_{avg}U + C_{avg}\tilde{x} + D_{avg}\tilde{u} + [(C_1 - C_2)X + (D_1 - D_2)U]\tilde{d} + [(C_1 - C_2)\tilde{x} + (D_1 - D_2)\tilde{u}]\tilde{d} \quad (2.6)$$

The terms:  $A_{avg}X + B_{avg}U$  and  $C_{avg}X + D_{avg}U$  represent the behaviour of the system in the steady state. There is one condition which needs to be considered that the the derivative of the steady state is zero i.e.  $\dot{X} = 0$ . Therefore the following equations are obtained:

$$0 = A_{avg}X + B_{avg}U \quad (2.7)$$

$$Y = C_{avg}X + D_{avg}U \quad (2.8)$$

Finally, the transfer functions for converters can be obtained between the input and the output. The Steady State Transfer Function calculated as,

$$\frac{Y(s)}{U(s)} = -C_{avg}[A_{avg}]^{-1}B_{avg} + D_{avg} \quad (2.9)$$

The steady state values can be then used to verify whether the model made is correct or not. The transfer function from the outputs to the inputs can be calculated as,

$$\frac{Y(s)}{U(s)} = C_{avg}[sI - A_{avg}]^{-1}B_{avg} + D_{avg} \quad (2.10)$$

## 2.3 PV string Modelling based on the information in datasheet

Since performance of solar PV is highly dependent on the environmental conditions i.e. irradiance and temperature, it is important to perform analysis which focuses on the characteristics of the solar PV devices in order to improve the energy production and the level of control to be established. By using the equivalent circuits, it becomes easier to analyse the performance of the cell/panel. Usually, modelling of solar panels is performed through numerical fitting to substantial experimental results. But, many small scale users cannot perform this since it is not affordable. As a result, analytical methods thus represent a solution to this problem, which require a small amount of information which can be found in the datasheet, making the process quite straightforward. By making the model in an accurate manner, it can be included in the mathematical model of the converter circuit, thus to examine its behaviour with varying operating conditions so that control can be established accordingly to extract the maximum power. PV panels are linked in series to create strings in PV power plants to provide a voltage level that fulfills the power processing system's input requirements. The required power level of the PV plant is achieved by connecting a number of strings in parallel, each consisting of the same number of panels, resulting in a rise in the PV field's current level. The current vs. voltage (I-V) characteristic of the entire PV field can be acquired by stretching that of a single cell, i.e. multiplying voltage values by the number of cells in series in each panel and then by the number of panels in each string. The cell current values are multiplied by the number of strings of panels connected in parallel. This voltage and current scaling up is only possible if all of the cells are identical and operate under identical operating circumstances, particularly in terms of irradiance and temperature **pvpowerbook1**.

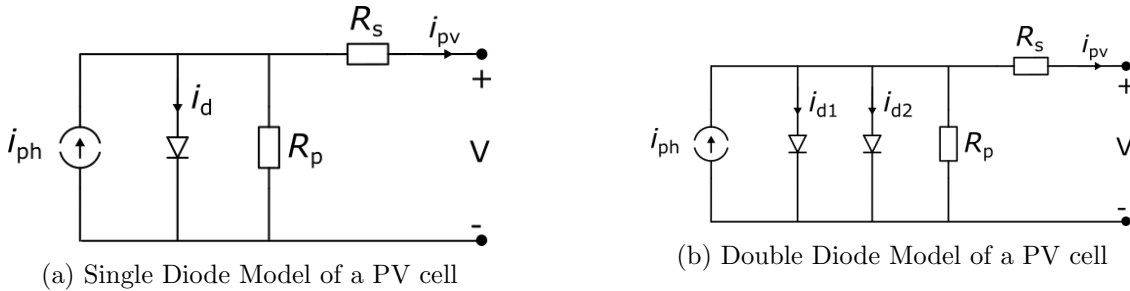


Figure 2.2: Single and Double Diode Models of a PV Panel

Figure 2.2a shows the most common circuit for a solar cell/panel, which contains a current source, one diode, and two resistors, one in series and the other in parallel. Here, the diode accounts for the physical phenomena that occur at the cell's silicon p-n junction. The photo-induced current is represented by the current source, which is linearly dependent on the cell area, irradiation level, and temperature, as well as the properties of the semiconductor material employed for the cell. Ideal solar cells, as is widely known, act as a current source coupled in series with a diode[9], [10], [11]. The ideality factor  $\eta$  is assumed to have a fixed value in the single diode equation. The voltage across the device actually affects the ideality factor.

The Figure 2.2b is the double diode model which has an extra diode. At higher voltage levels, the surface and the bulk regions are the ones that govern the recombination occurring in the cell. This brings the ideality factor close to one. Whereas at low voltage, the dominance of the recombination in the junction is what brings the ideality factor close to two. Addition of the second diode is performed in order to model the recombination occurring at the junction[12]. This simple equivalent circuit accurately reproduces the current-voltage curve of a solar cell or panel, referred to as the I-V curve 2.3. It also depicts two points on the I-V curve: short circuit and open circuit. Similarly, a power-voltage curve is also present to obtain the maximum power point under the Standard Testing Conditions (STC) The standard information supplied in manufacturers' datasheets is these representative points,

as well as their fluctuation as a function of temperature.

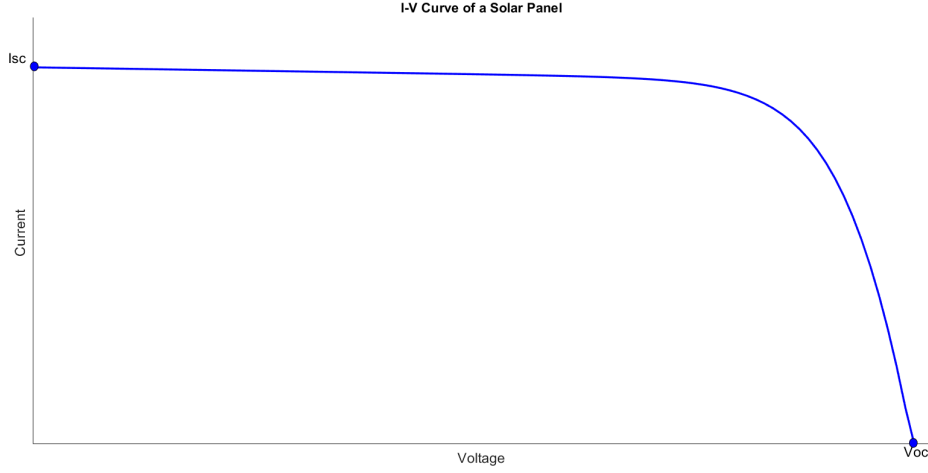


Figure 2.3: I-V Curve of a PV Panel

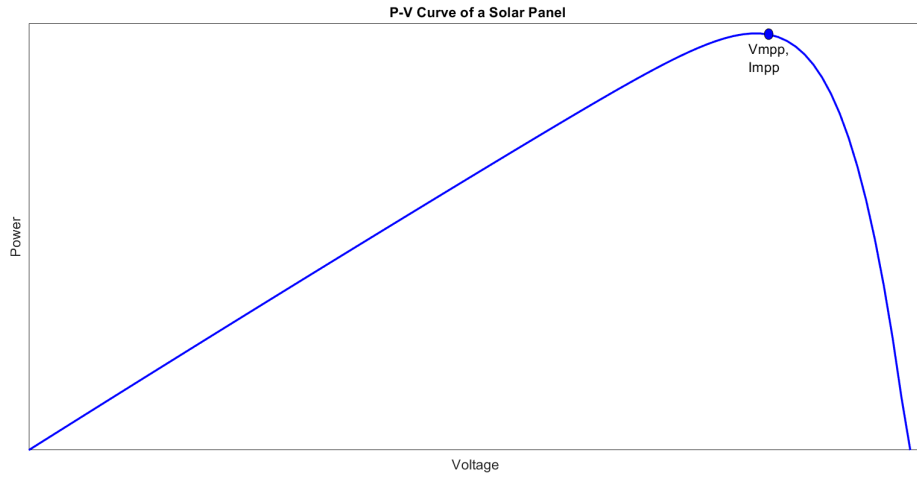


Figure 2.4: P-V Curve of a PV Panel

An analytical method based on a limited amount of data has been devised in[13]. It includes standard manufacturer data as well as the derivation of four equations to calculate series resistance  $R_s$ , shunt resistance  $R_{sh}$ , saturation current  $I_s$ , and photo current  $I_{ph}$ . [14] proposes an iterative approach for obtaining these parameters, along with the Ideality factor  $\eta$  which is a material dependent quantity and is necessary to calculate the other parameters. Although different technologies are associated with varying values of the aforementioned ideality factor under normal conditions, some authors propose a generic value in the bracket [1, 1.5] for every type of cell. Following equation of the current  $I$  and voltage  $V$  can be used to mode the equivalent circuit of the single diode model.

$$I = I_{ph} - I_o \left( \exp \left( \frac{V + IR_s}{\eta \cdot N_s \cdot V_{th}} \right) - 1 \right) - \frac{V + IR_s}{R_p} \quad (2.11)$$

where  $I_{ph}$  is the photo-generated current,  $I_o$  is the saturation current,  $N_s$  is the number of cells connected in series and  $V_{th} = \frac{k_B T}{q}$  is the thermal voltage, where  $k_B$  is the Boltzmann's constant,  $T$  is the temperature ( $^{\circ}K$ ) and  $q$  is the elementary charge. Now, to calculate the five parameters

$\eta, I_{ph}, I_{sat}, R_s$  and  $R_p$  the following information is required from the datasheet. The datasheet of the PV module provides the information under the standard testing conditions (STC)

- The open circuit voltage:  $V_{oc}$
- Short circuit current:  $I_{sc}$
- Maximum power point voltage:  $V_{mpp}$
- Maximum power point current:  $I_{mpp}$
- Open circuit voltage/temperature coefficient:  $K_v$
- Short circuit current/temperature coefficient:  $K_i$

### Ideality Factor ( $\eta$ )

According to [15] the Ideality factor can be calculated using the equation 2.12.  $E_g$  and  $T_{ref}$  are the band gap energy and temperature under STC.

$$\eta = \frac{K_v - \frac{V_{oc}}{T_{ref}}}{N_s V_{th} \left( \frac{K_i}{I_{sc}} - \frac{3}{T_{ref}} - \frac{E_g}{k_b T_{ref}^2} \right)} \quad (2.12)$$

### Saturation Current ( $I_{sat}$ )

The saturation current can be calculated as

$$I_{sat} = I_{sc} \cdot \exp\left(-\frac{V_{oc}}{\eta \cdot N_s \cdot V_{th}}\right) \quad (2.13)$$

### Series Resistance ( $R_s$ )

Here, the ideality factor, the short circuit current and the open circuit current are the required parameters to calculate  $R_s$  using the following steps. Under Open circuit and Short circuit conditions the equations are

$$0 = I_{ph} - I_{sat} \left( \exp\left(\frac{V_{oc}}{\eta \cdot N_s \cdot V_{th}}\right) - 1 \right) - \frac{V_{oc}}{R_p} \quad (2.14)$$

$$I_{sc} = I_{ph} - I_{sat} \left( \exp\left(\frac{I_{sc} R_s}{\eta \cdot N_s \cdot V_{th}}\right) - 1 \right) - \frac{I_{sc} R_s}{R_p} \quad (2.15)$$

According to [16] the negative bifurcation of Lambert W can be used to calculate the value of  $R_s$

$$R_s = \alpha [W_{-1}(\beta \exp(\gamma)) - (\delta + \gamma)] \quad (2.16)$$

where,

$$\alpha = \frac{\eta \cdot N_s \cdot V_{th}}{I_{mpp}} \quad (2.17)$$

$$\beta = -\frac{V_{mpp}(2I_{mpp} - I_{sc})}{(V_{mpp}I_{sc} + V_{oc}(I_{mpp} - I_{sc}))} \quad (2.18)$$

$$\gamma = -\frac{2V_{mpp} - V_{oc}}{\eta N_s V_{th}} + \frac{((V_{mpp} * I_{sc}) - (V_{oc} * I_{mpp}))}{((V_{mpp}I_{sc} + V_{oc}(I_{mpp} - I_{sc}))} \quad (2.19)$$

$$\delta = \frac{V_{mpp} - V_{oc}}{\eta N_s V_{th}} \quad (2.20)$$

### Shunt Resistance (Rsh)

Similarly, the equations for  $R_{sh}$  can be given as

$$R_{sh} = \frac{(V_{mpp} - I_{mpp}R_s)(V_{mpp} - R_s(I_{sc} - I_{mpp}) - \eta N_s V_{th})}{(V_{mpp} - I_{mpp}R_s)(I_{sc} - I_{mpp}) - \eta N_s V_{th} I_{mpp}} \quad (2.21)$$

### Diode Dynamic Resistance (Rd)

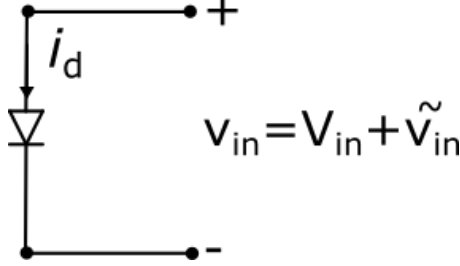


Figure 2.5: Diode in the model of the PV generator

To model the dynamic behaviour of the PV generator, the dynamic resistance of the same has to be considered and evaluated. It has to be included in the model of the complete system. Small signal analysis can be performed in order to evaluate this dynamic resistance. The voltage across the diode  $v_{in}$  and the current through the diode  $i_d$  can be expressed as

$$v_{in} = V_{in} + \tilde{v}_{in} \quad i_d = I_{sat}(e^{\eta \frac{v_{in}}{V_{th}}} - 1) = I_d + \tilde{i}_d \quad (2.22)$$

where  $\tilde{v}_{in}$  and  $\tilde{i}_d$  are the small signal variations. Since the PV model has a current source with a diode in parallel, in order to integrate the PV model in the State Space Model of DC-DC Converter, a Taylor series approximation can be used to linearize the behaviour of the diode for the considered operating conditions.

$$f(x) = \sum_0^{\infty} \frac{1}{m!} \frac{\partial^m f(x)}{\partial x^m} \Big|_{x=X} (x - X)^m \quad (2.23)$$

$$f(x) = f(X) + \frac{\partial f(x)}{\partial x} \Big|_{x=X} (x - X)^m \quad (2.24)$$

where  $x = X + \tilde{x}$  is the operating point at which the model is linearized. Now this Taylor series expression has been used on the diode current equation mentioned above to calculate the dynamic resistance of the diode at the specific operating point.

$$i_d(v_{in})|_{v_{in}=V_{in}} = i_d(V_{in}) + \frac{\partial i_d(v_{in})}{\partial (v_{in})} \Big|_{v_{in}=V_{in}} \quad (2.25)$$

After expansion of this expression at the operating point denoted by  $V_{in}$ , the outcome is,

$$i_d(v_{in})|_{v_{in}=V_{in}} = I_{sat}(e^{\eta \frac{V_{in}}{V_{th}}} - 1) + \frac{I_{sat}}{\eta V_{th}} \times e^{\eta \frac{V_{in}}{V_{th}}} \times \tilde{v}_{in} \quad (2.26)$$

where  $I_{sat}(e^{\eta \frac{V_{in}}{V_{th}}} - 1)$  is the Steady state quantity and  $\frac{I_{sat}}{\eta V_{th}} \times e^{\eta \frac{V_{in}}{V_{th}}} \times \tilde{v}_{in}$  is the small signal variation.

By rearranging the terms in the term that represents the small signal variations, the dynamic resistance of the diode can be calculated for a particular operating point, which is stated as

$$R_d = \frac{\eta V_{th}}{I_{sat}} \times e^{-\frac{V_{in}}{\eta V_{th}}} \quad (2.27)$$

## 2.4 Modern PV based systems

Over the years PV has gained a lot of importance in investment and research fields. Contemporary PV technologies and materials have given rise to cells that are less expensive, more efficient, and produce a lot of electricity per square meter [17]. A photovoltaic (PV) system is made up of strings of solar panels and the output of it is stepped up or stepped down by a converter circuit, and supplied to an electrical equipment depending on the demand. PV systems come in a wide range of sizes, from little rooftop or portable units to enormous utility-scale power plants. Grid-connected PV-based systems and Standalone PV-based systems are the two primary categories of PV-based systems. Standalone PV systems, also known as off-grid systems, typically function independently of the utility grid. It is clear that we anticipate a match between supply and demand, or more specifically between the size of the PV system and the power requirements of the load. A PV based storage system is needed for a different kind of stand-alone so that extra energy may be stored for later use. Such type of systems can be directly linked to DC loads or connected to AC loads through an inverter circuit.

The Hybrid PV System, which is another typical form of standalone system, employs other energy sources in addition to the PV array to power loads. These power sources can include fuel cells, diesel generators, hydro turbines, wind turbines, and hydro turbines. Batteries are another option for energy storage in hybrid PV systems. For situations where customers wish to reduce their energy costs and while the utility grid is still available for usage when the PV array is not producing any electricity, this form of setup is the most typical. The PV array can be directly connected to the grid without the use of a storage system and is known as a Grid-Tied PV System. It may also store surplus energy in battery banks for later use, in which case it is known as a Bimodal PV System[18].

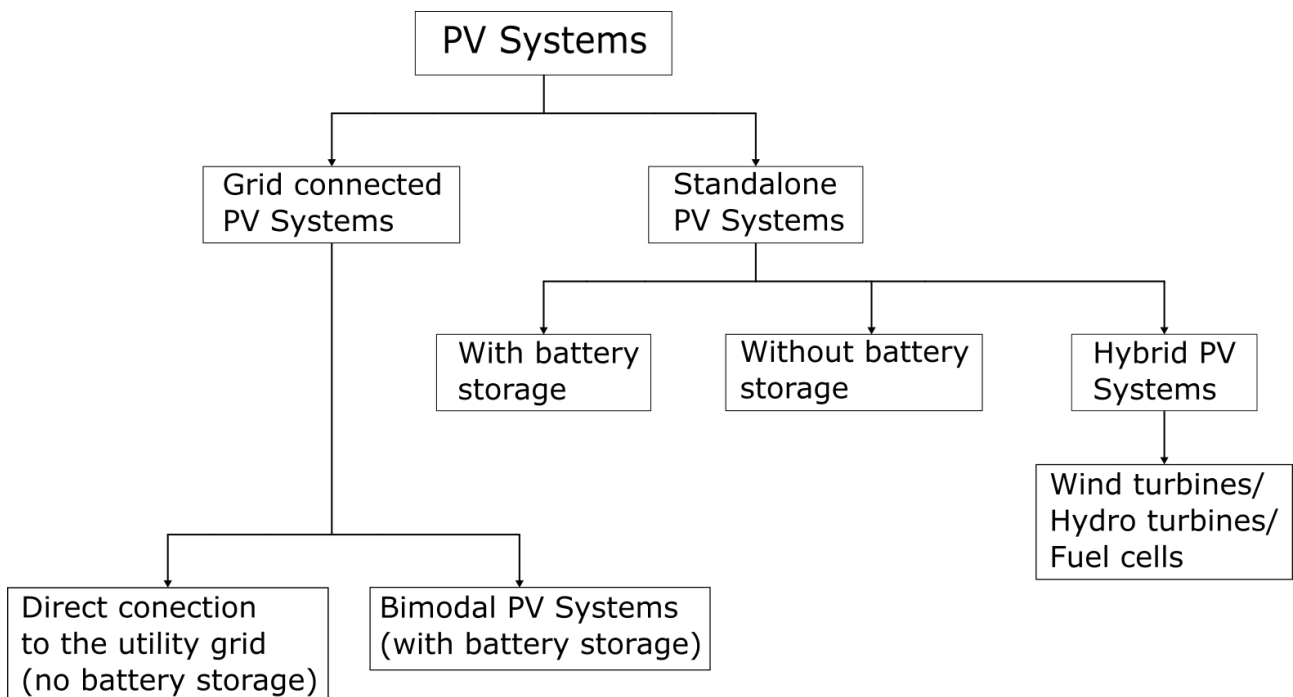


Figure 2.6: Different types of PV systems [18]

## 2.5 DC Microgrids, DC-DC Converters and Control

A microgrid is a self-contained collection of DER capable of both islanding and grid connected functioning. The comparison of the DC and AC Microgrids is usually done in terms of distribution line losses, protection, power converters, power quality and control complexity [19].

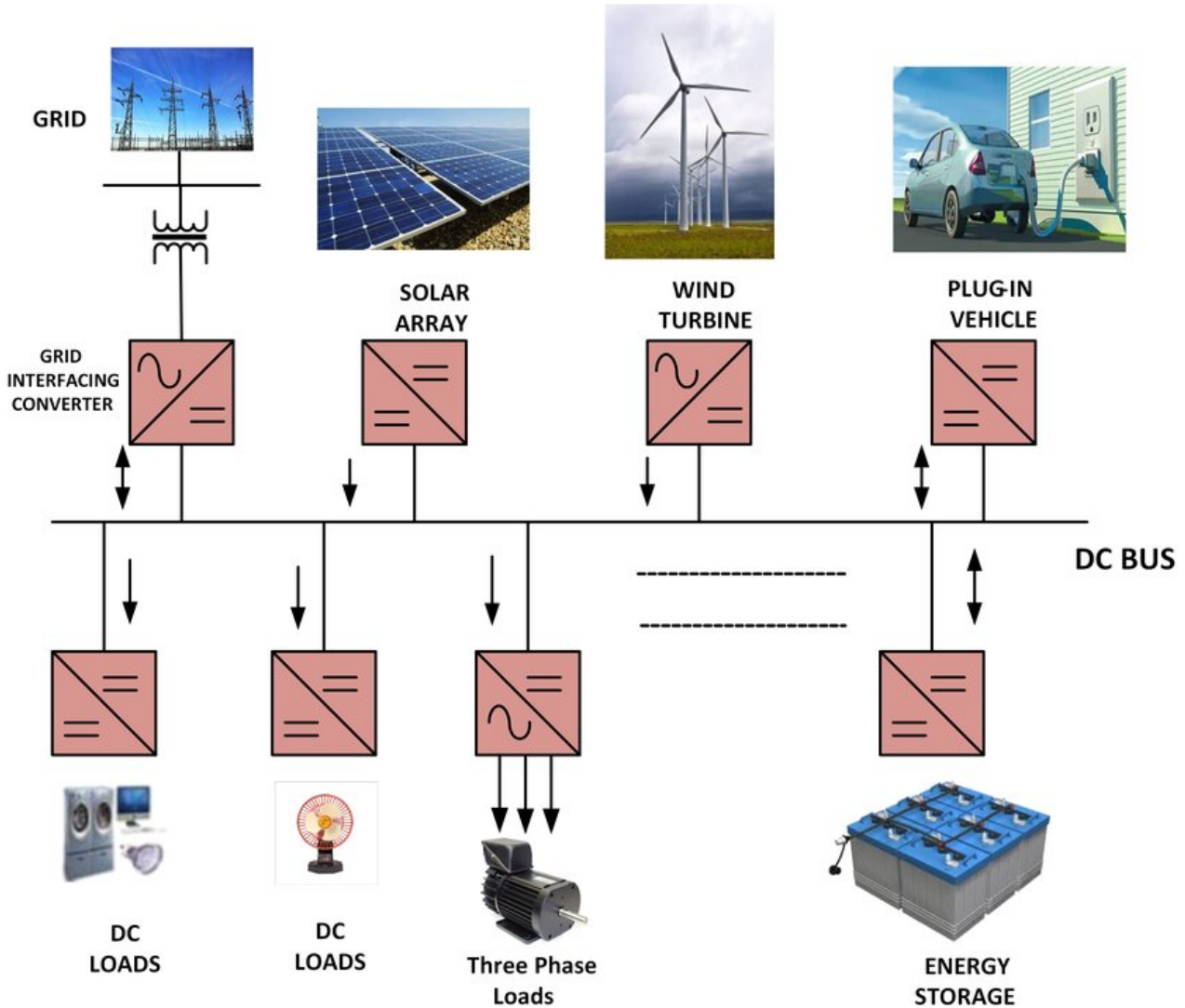


Figure 2.7: Typical configuration of a DC Microgrid [20]

Microgrid research and studies were initially conducted to conform to existing AC grid standards and to address ac-power-related issues such as power quality. This was mostly owing to technology limitations and circumstances at the time. The transformer is the most important component of the traditional AC grid, and its ability to change voltage levels efficiently in order to move centrally bulk produced power to the transmission voltage level and then back to the distribution voltage level was the reason for AC power becoming the norm in power systems. HVDC systems primarily employed DC to link various AC networks or for industrial applications [21]. All of the advances in power electronics have allowed low-cost, high-efficiency DC/DC converters, which, because to their greater switching frequency compared to their AC equivalents, result in fewer components, lower losses, lower harmonics, and lower prices [22].

Furthermore, DC microgrids have gained popularity in recent years as a result of the introduction of Distributed Energy Resources (DERs) such as solar photovoltaic (PV), fuel cells, and various DC loads, as well as the high-level integration of various energy storage systems such as batteries and

supercapacitors [23]. Simultaneously, the skin effect is reduced, allowing for a higher power level. In comparison to the AC version, the same principles apply in the distribution lines, allowing for larger local loads to be delivered. Finally, a growth in electronic loads such as computers, cellphones, and other electronic devices that are natively DC or utilize an integrated rectification (ac to dc) stage to run at the appropriate dc voltage or require a dc link to the grid. LED lights, variable frequency machines such as refrigerators, air conditioners, heaters, , and variable-frequency drive machines are examples of such loads [24]. A direct dc connection will assist all of these since it will eliminate the requirement for several conversion stages.

However, assuring user safety in DC systems remains a significant problem, owing to a lack of practical experience compared to AC systems, which have been deployed and tested in a wide range of applications for over a century. The waveform of the current in DC is the weakest point of the protection systems, as it never crosses zero, making the design of short-circuit breakers more complex. Typical AC circuit breakers can, however, be utilized in low DC voltage applications if their power ratings are modified for DC . The waveform of the current in DC is the weakest point of the protection systems, as it never crosses zero, making the design of short-circuit breakers more complex. Typical AC circuit breakers can, however, be utilized in low DC voltage applications if their power ratings are modified for DC [25].

But progress has been happening to develop better solid state protection systems for DC Microgrids. As a result, it makes sense to run a microgrid in DC and link all of the components to a common DC bus through DC converters. Due to the absence of synchronization for frequency and phase, reactive power management, and fewer harmonics, a DC Microgrid offers better reliability, high efficiency with appropriate voltage level, and good performance. These grids can work in tandem with the main grid using bidirectional AC-DC converters, improving the main grid’s dependability by facilitating supply and demand power balance[24].

### 2.5.1 Control of DC-DC Converters

DC-DC converters are one of the most extensively utilized electronic circuits in power electronics based applications [26]. With the evolution of DC-microgrids, the DC-DC converters have made immense progress to provide a better functionality. For example, the step Buck or Boost converters used in various applications where DERs are present, the DC-DC bidirectional converters which help in the integration of Electric Vehicles with a standalone microgrid, thus making them a source of power when the renewable sources/main grid are unavailable, the AC-DC bidirectional converters which help in the integration of Electric Vehicles in microgrids that are connected to a main grid. Depending on the demand of the load the step up/ step down actions are carried out in the converters to provide the power to the load. DC microgrids supply various loads of different power requirements. These loads can be of constant or varying power requirements and it is necessary to keep the demand fulfilled without any inconsistency and instability. Therefore establishing fast, stable and reliable control is a necessity. The fundamental issue with DC-DC converter functioning is an uncontrolled power source, which causes DC-DC converters to malfunction. There are a variety control techniques which have been adopted by industry depending on the load, power requirements, the converter topology and nature of operation[27].

### Maximum Power Point Tracking Algorithms

The maximum power generated by photovoltaic panels is not always constant at the same operating point; it changes depending on meteorological factors including sun irradiation and temperature. To get the most power out of the system, an MPPT algorithm that optimizes the power extraction dynamically is generally used. One of the most essential characteristics of all MPPT algorithms is convergence speed. Any improvement in the time taken to reach the MPP enhances the system’s dependability and boosts the power extraction of the entire system [28].

**Perturb and Observe (P&O):** P&O uses an iterative approach. Periodically, it senses the panel's operating voltage and current to calculate the power change ( $\Delta P_{PV}$ ) that results from comparing the PV current output power to the preceding power. The perturbation in the operational voltage should be in the same direction as the increment if ( $\Delta P_{PV}$ ) is positive. The system operating point, however, shifts away from the MPPT if it is negative, and the operating voltage should be in the opposite direction as the increment. The perturbation should then be reversed to move back towards the MPP. Regardless of the irradiance and terminal voltage of the PV module, this process continues until  $\frac{\partial P_{pv}}{\partial V_{pv}} = 0$  [29]. Thus the P&O algorithm oscillates around the point where the derivative of the power with respect to the voltage is zero. In **pvpowerbook1** the Mathematical Equation for the P&O algorithm is mentioned as

$$x_{(k+1)T_{Perturb}} = x_{(k)T_{Perturb}} \pm (x_{(k)T_{Perturb}} - x_{(k-1)T_{Perturb}}) \times (\pm(P_{(k)T_{Perturb}} - P_{(k-1)T_{Perturb}})) \quad (2.28)$$

where,

- $x$ : Parameter to be perturbed
- $T_{Perturb}$  (Perturbation time): Duration of time between two perturbations

Another important factor in the P&O algorithm is the perturbation amplitude  $\Delta x$ . The perturbation time  $T_{Perturb}$  and the perturbation amplitude both are inversely proportional to each other. The basic P&O algorithm uses a fixed step. Thus by selecting an appropriate interval for  $T_{Perturb}$ , a stable three point operation can be obtained **pvpowerbook1**.

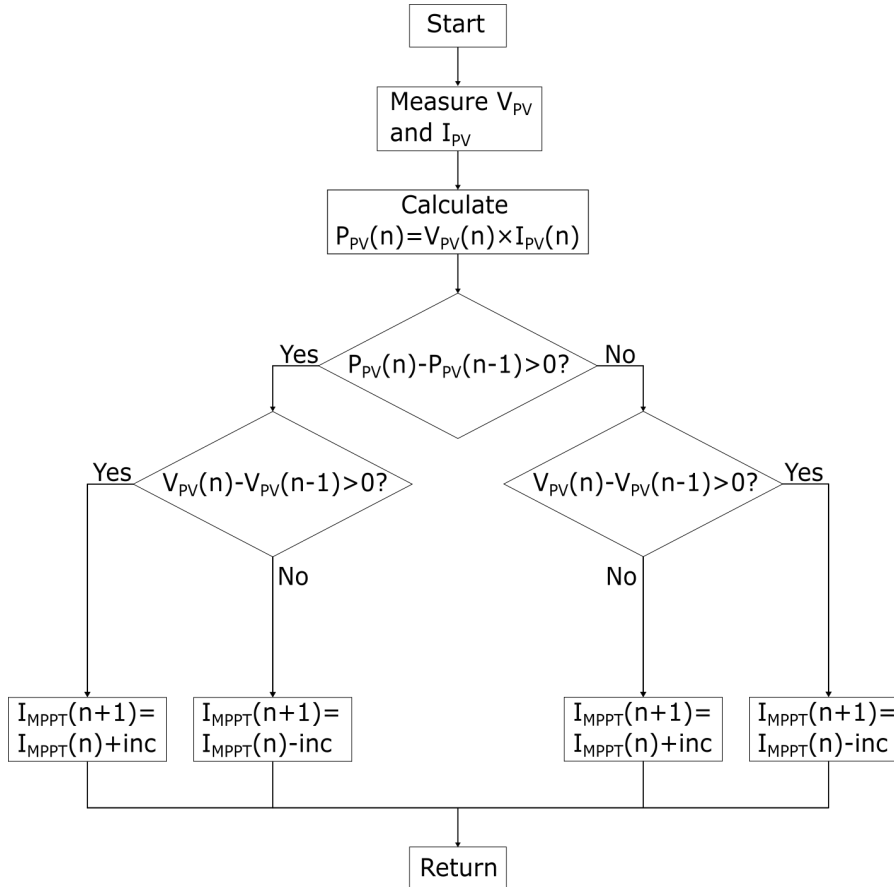


Figure 2.8: Flowchart of Perturb and Observe MPPT Algorithm

Figure 2.8 shows the flowchart of how the P&O MPPT Algorithm functions. The PV generated voltage and current values i.e.  $V_{pv}$  and  $I_{pv}$ . Then the newly calculated power  $P_n$  is compared to the

power calculated in the previous iteration i.e.  $P_{n-1}$  to calculate the  $\Delta P$ . Then depending on the  $\Delta P$  and  $\Delta V$ , MPP is tracked.

**Incremental Conductance:** The incremental conductance approach is based on the idea that the power curve of the PV array has zero slope at the MPP, causing  $\Delta P/\Delta V = 0$  and  $P = VI$ . This results into the three conditions for keeping the maximum power point constant, which are:

$$\frac{\Delta I}{\Delta V} = -\frac{I}{V}; \text{if } P = MPP \quad \frac{\Delta I}{\Delta V} > -\frac{I}{V}; \text{if } P < MPP \quad \frac{\Delta I}{\Delta V} < -\frac{I}{V}; \text{if } P > MPP$$

By comparing the incremental conductance  $\Delta I/\Delta V$  with the instantaneous conductance  $I/V$ , the MPP may be monitored.

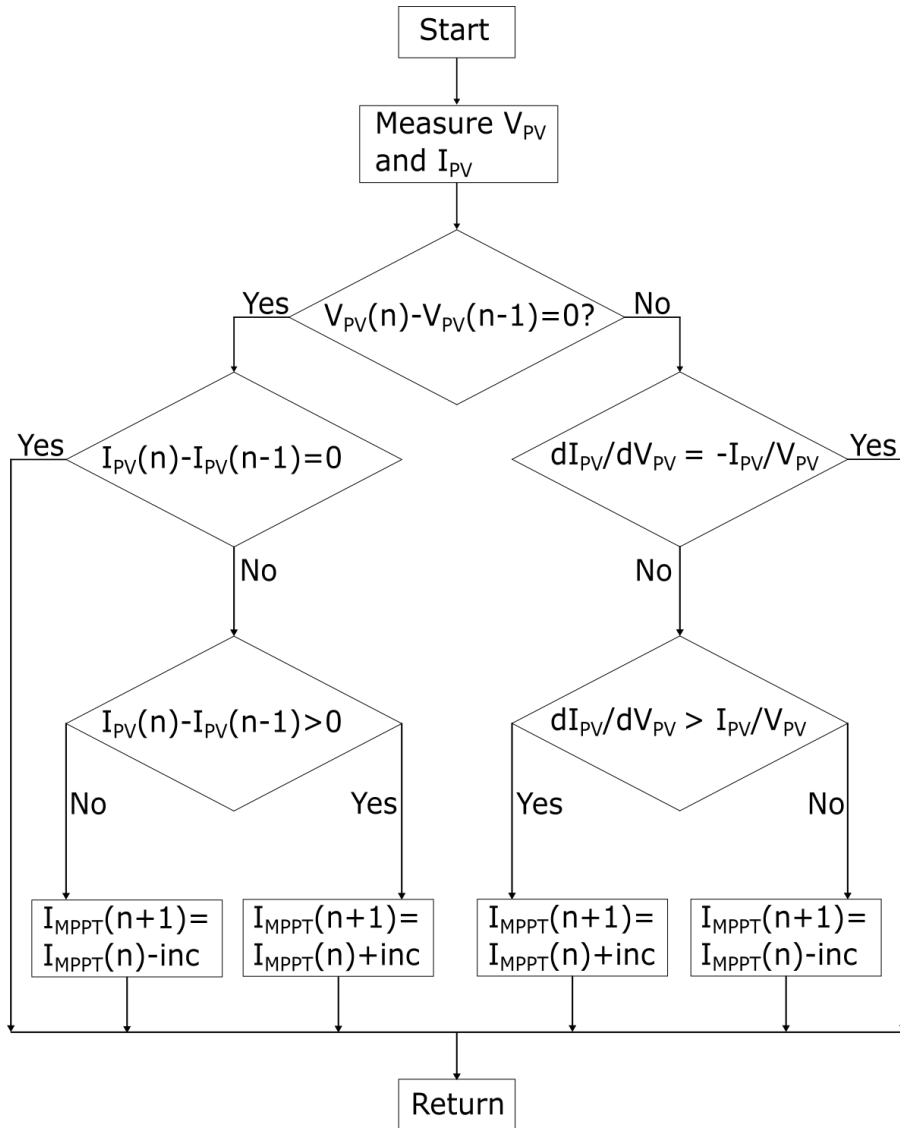


Figure 2.9: Flowchart of Incremental Conductance MPPT Algorithm

The method moves the reference up or down until the requirement  $\Delta I/\Delta V = -I/V$  is met. The functioning of the PV array is continued until the maximum power has been attained. High sample rates and quick power slope computations are necessary for this efficient technique [28][30].

## Droop Control

Higher level control is not necessary for an islanded DC Microgrid with few components, like in this thesis. Power balancing, which is accomplished by correct voltage regulation and current sharing among the parallel converters of the power sources, storage units, and in unusual circumstances even loads, activities carried out by the primary/local control, is the key problem, as we noted, in this operation[24]. Droop control is a method designed to reduce the low DC output impedance of power converters, which is the main factor contributing to inefficient load sharing. The basic tenet of droop control is to lower the converter voltage output when the current is increased.. This introduces a resistive characteristic into the system. A series resistor may be used to provide droop control in each paralleled converter, however doing so comes at a considerable cost in power losses [31]. The common droop technique is described in the the form of droop resistance as

$$V_{out} = V_{NL} - I_{out} \times R_{droop} \quad (2.29)$$

where,  $R_{droop}$ ,  $I_{out}$ ,  $V_{out}$ ,  $V_{ref}$  are droop coefficient which is a virtual resistance, converter output current, converter output voltage and the no load voltage respectively. Since the droop coefficient is essentially a virtual resistance, it enables current sharing and voltage regulation in the DC Microgrid. The slope of the curve is represented by the droop coefficient. According to 2.29, a low droop coef-

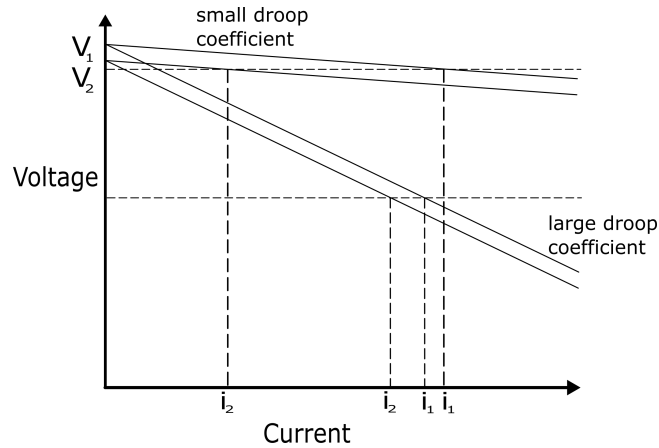


Figure 2.10: Droop Control

ficient indicates a minor variation in the DC bus voltage, but at the expense of inadequate current sharing between converters. On the other hand, as shown in Figure 2.10, a high droop coefficient improves load sharing but also leads to substantial voltage variations. This is primarily caused by load distribution and error sensing in the voltage measurement, where typically uneven cable resistances superimpose over the droop coefficient and lead to distinct droop equations [32].

[24] states that by changing the droop voltage equation appropriately, a distributed secondary control is being used in [32] and [33] to suppress the voltage deviation. The needed voltage shift for the voltage equations is processed in a secondary control loop in which a controller uses average current sharing techniques to distribute low-bandwidth load information to the other converters. The non-linear droop is an additional option where

$$V_{out} = V_{NL} - K \times I_{out} \quad (2.30)$$

Here, the droop coefficient  $K$  is variable depending on the conditions on the load side but communication is another requirement[24].

---

State Space Modelling of MPPT converters

---

This section describes the mathematical models made of multiple DC-DC converters. It includes the state space model of the Boost Converter for tram lines and a state space model of a Boost converter for a Bipolar DC Microgrid. The state space models have been made of both these converters in order to implement control on both of them. Both the converters have PV strings connected to their inputs and the model of those PV strings have been included at the input side of the converters. This has been done in order to understand the dynamics of the solar PV string and establish the control accordingly. In order to provide a regulated output to the grid while avoiding instability, establishing a fast control on the active switch is an important task. One of the most important methodologies for studying switched mode power conversion circuits is state-space averaging (SSA). State space models may also make transient analysis go considerably faster. It also contributes in the integration of control. The control algorithm determines the required input voltage and current to the converter thus maximizing the generation of the PV string. Initially the model of the basic boost converter has been made, followed by the model of the converter for the bipolar DC Microgrid. Another reason for making the mathematical model of the converter for the Bipolar grid is that DC distribution grids and microgrids are expected to expand due to increasing number of DC loads and lesser losses as compared to AC. The approach of making the models of the converters has been adopted from Section 2.2 and the model of the PV has been made based on the approach mentioned in Section 2.3.

### 3.1 Boost Converter for the tram lines

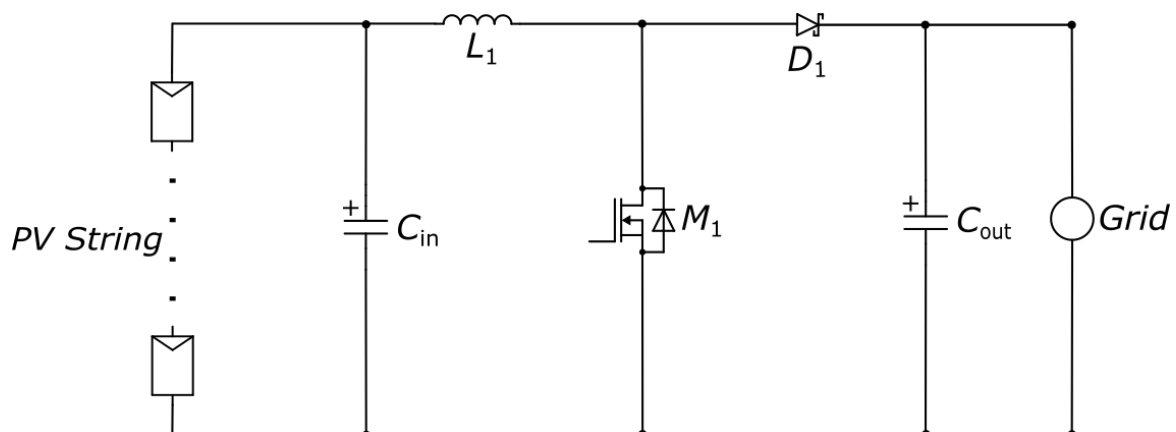


Figure 3.1: Grid connected Boost Converter with PV as the input

The above figure shows the circuit of a Boost converter. Here the MOSFET is the active switch. During the turn on time  $T_{on}$  the MOSFET is turned on and the inductor charges. And, during the off time  $T_{off}$  MOSFET turns off and the current flows through the diode to the output. The on-time in the form of duty cycle (D) is the ratio of on-time to the total switching period i.e.  $D = T_{on}/T_s$ . The analysis has been performed in Continuous Conduction Mode (CCM). The duty cycle (D) and the inductor current ripple ( $\Delta I_L$ ) can be calculated as follows

$$D = 1 - \frac{V_{in}}{V_o} \qquad \Delta I_L = \frac{V_{in}D}{f_s L} \qquad \text{where,}$$

- $V_{in}$  = Input Voltage
- $V_o$  = Output Voltage
- $f_s$  = Switching Frequency

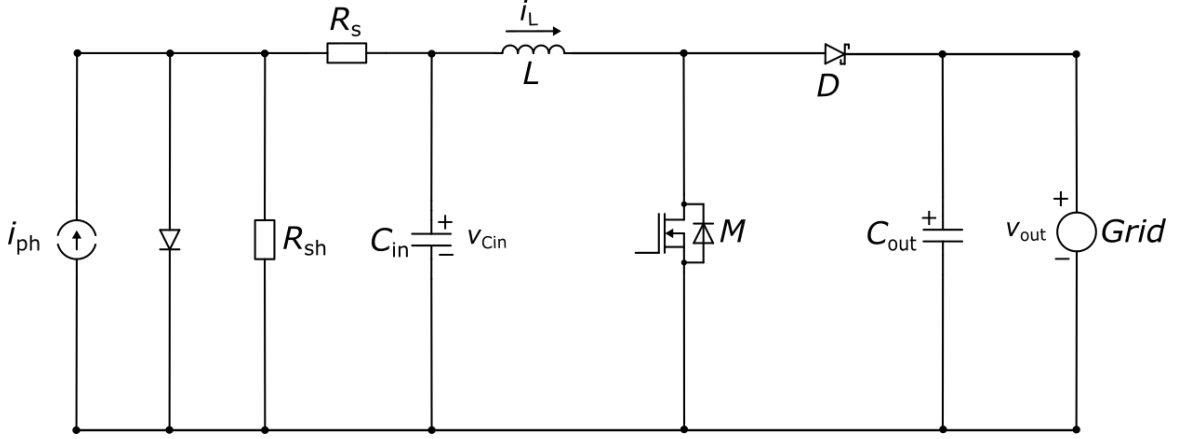


Figure 3.2: PV powered Boost Converter for tram lines with PV model at its input

The above figure 3.2 shows the circuit used for making the state space model. As seen in this figure, the PV model of the string has been included at the input of this converter. The resistances  $R_s$ ,  $R_{sh}$  and  $R_d$  have been calculated using the modelling method mentioned earlier. The variations in the diode resistance are temperature dependent and effect of temperature has not been considered in this thesis, thus the diode resistance has been calculated for MPP values for the STC. Since  $R_d$  and  $R_{sh}$  are parallel to each other, and the model has been made for the MPP under STC, the resistance in parallel to the current source is calculated by performing  $R_{sh}||R_d$  and will be referred to as  $R_P$ . Also, the term  $i_{ph}$  used for modelling here is  $i_{ph} - i_{diode,DC}$ . Therefore the model made is valid when  $R_P = R_{sh}||R_d$ . Control strategy has to be implemented at the input side of the converter, since the converter is connected to a grid at the output side which powers the trams when required. The State and the Output Parameters considered are inductor current ( $i_L$ ) and input side capacitance ( $v_{c_{in}}$ ). The Input Parameters considered are the current generated by the PV source ( $i_{ph}$ ) and the output side voltage ( $v_o$ ). The State (x), Input (u) and the Output (y) parameters considered for modelling are:

$$x = \begin{pmatrix} i_L \\ v_{c_{in}} \end{pmatrix} \qquad u = \begin{pmatrix} i_{ph} \\ v_o \end{pmatrix} \qquad y = \begin{pmatrix} i_L \\ v_{c_{in}} \end{pmatrix} \qquad (3.1)$$

For the ON TIME, using KVL and KCL, the State Equation and the Output Equation can be men-

tioned as

$$\begin{pmatrix} \dot{i}_L \\ \dot{v}_{c_{in}} \end{pmatrix} = \begin{pmatrix} 0 & \frac{1}{L} \\ \frac{-1}{C_{in}} & \frac{-1}{R_P C_{in} (1 + \frac{R_S}{R_P})} \end{pmatrix} \begin{pmatrix} i_L \\ v_{c_{in}} \end{pmatrix} + \begin{pmatrix} 0 & 0 \\ 0 & \frac{1}{C_{in} (1 + \frac{R_S}{R_P})} \end{pmatrix} \begin{pmatrix} i_{ph} \\ v_o \end{pmatrix} \quad (3.2)$$

$$\begin{pmatrix} i_L \\ v_{c_{in}} \end{pmatrix} = \begin{pmatrix} 1 & 0 \\ 0 & 1 \end{pmatrix} \begin{pmatrix} i_L \\ v_{c_{in}} \end{pmatrix} + \begin{pmatrix} 0 & 0 \\ 0 & 0 \end{pmatrix} \begin{pmatrix} i_{ph} \\ v_o \end{pmatrix} \quad (3.3)$$

thus representing  $\dot{x} = A_1 x + B_1 u$  and  $y = C_1 x + D_1 u$  in their respective and accurate manner. For the OFF TIME, using KVL and KCL, the State Equation and the Output Equation can be mentioned as

$$\begin{pmatrix} \dot{i}_L \\ \dot{v}_{c_{in}} \end{pmatrix} = \begin{pmatrix} 0 & \frac{1}{L} \\ \frac{-1}{C_{in}} & \frac{-1}{R_P C_{in} (1 + \frac{R_S}{R_P})} \end{pmatrix} \begin{pmatrix} i_L \\ v_{c_{in}} \end{pmatrix} + \begin{pmatrix} \frac{-1}{L} & 0 \\ 0 & \frac{1}{C_{in} (1 + \frac{R_S}{R_P})} \end{pmatrix} \begin{pmatrix} i_{ph} \\ v_o \end{pmatrix} \quad (3.4)$$

$$\begin{pmatrix} i_L \\ v_{c_{in}} \end{pmatrix} = \begin{pmatrix} 1 & 0 \\ 0 & 1 \end{pmatrix} \begin{pmatrix} i_L \\ v_{c_{in}} \end{pmatrix} + \begin{pmatrix} 0 & 0 \\ 0 & 0 \end{pmatrix} \begin{pmatrix} i_{ph} \\ v_o \end{pmatrix} \quad (3.5)$$

thus representing  $\dot{x} = A_2 x + B_2 u$  and  $y = C_2 x + D_2 u$  in their respective and accurate manner. Once this set of equations is obtained, the averaging procedure is performed by multiplying all the ON TIME matrices with duty cycle  $\mathbf{d}$  and the OFF TIME matrices are multiplied with  $\mathbf{1} - \mathbf{d}$  performing the averaging procedure.

$$\begin{aligned} A_{avg} &= A_1 \times d + A_2 \times (1 - d) \\ B_{avg} &= B_1 \times d + B_2 \times (1 - d) \\ C_{avg} &= C_1 \times d + C_2 \times (1 - d) \\ D_{avg} &= D_1 \times d + D_2 \times (1 - d) \end{aligned} \quad (3.6)$$

The averaged matrices calculated are

$$A_{avg} = \begin{pmatrix} 0 & \frac{1}{L} \\ \frac{-1}{C_{in}} & \frac{-1}{R_P C_{in} (1 + \frac{R_S}{R_P})} \end{pmatrix} \quad B_{avg} = \begin{pmatrix} \frac{-(1-d)}{L} & 0 \\ 0 & \frac{1}{C_{in} (1 + \frac{R_S}{R_P})} \end{pmatrix} \quad (3.7)$$

$$C_{avg} = \begin{pmatrix} 1 & 0 \\ 0 & 1 \end{pmatrix} \quad D_{avg} = \begin{pmatrix} 0 & 0 \\ 0 & 0 \end{pmatrix} \quad (3.8)$$

After the averaging procedure is complete, signal perturbations are added to all the state, input and output parameters and the duty cycle. The capital letters indicate the Steady State terms and the letters with tilde on them indicate the small signal perturbations, for example  $i_L = I_L + \tilde{i}_L$ .

$$x = \begin{pmatrix} I_L + \tilde{i}_L \\ V_{c_{in}} + \tilde{v}_{c_{in}} \end{pmatrix} \quad u = \begin{pmatrix} I_{ph} + \tilde{i}_{ph} \\ V_o + \tilde{v}_o \end{pmatrix} \quad y = \begin{pmatrix} I_L + \tilde{i}_L \\ V_{c_{in}} + \tilde{v}_{c_{in}} \end{pmatrix} \quad (3.9)$$

$$A_{avg} = \begin{pmatrix} 0 & \frac{1}{L} \\ \frac{-1}{C_{in}} & \frac{-1}{R_P C_{in} (1 + \frac{R_S}{R_P})} \end{pmatrix} \quad B_{avg} = \begin{pmatrix} \frac{-(1 - (D + \tilde{d}))}{L} & 0 \\ 0 & \frac{1}{C_{in} (1 + \frac{R_S}{R_P})} \end{pmatrix} \quad (3.10)$$

$$C_{avg} = \begin{pmatrix} 1 & 0 \\ 0 & 1 \end{pmatrix} \quad D_{avg} = \begin{pmatrix} 0 & 0 \\ 0 & 0 \end{pmatrix} \quad (3.11)$$

After the addition of signal perturbations, the equations are written in the format as shown in equations 2.5 and 2.6, to calculate the Transfer Functions between the output and the input parameters. The small signal state-space averaged equations are written as

$$\dot{\tilde{x}} = A_{avg}\tilde{x} + B_{avg}\tilde{u} + [(A_1 - A_2)X + (B_1 - B_2)U]\tilde{d} \quad (3.12)$$

$$\tilde{y} = C_{avg}\tilde{x} + D_{avg}\tilde{u} + [(C_1 - C_2)X + (D_1 - D_2)U]\tilde{d} \quad (3.13)$$

where,  $A_{avg}, B_{avg}, C_{avg}, D_{avg}$  represent the steady state matrices. The Transfer Function from output to duty cycle can be calculated as,

$$\frac{\tilde{y}(s)}{\tilde{d}(s)} = C_{avg}[sI - A_{avg}]^{-1}[(A_1 - A_2)X + (B_1 - B_2)U] + [(C_1 - C_2)X + (D_1 - D_2)U] \quad (3.14)$$

### 3.1.1 Application in the project

The panel considered for use here is LG410N2W-L5 from the LG N2 series. A PV string would be connected at the input of the converter circuit shown in Figure 3.1 and thus integration of the model of the string would help to understand the dynamics in a better manner. The electrical specifications of this panel are mentioned in table 3.1.

Table 3.1: LG N2 series' LG410N2W-L5 panel

Specification Parameter	Value
Maximum Power (Pmax) (Wp)	410
MPP Voltage (Vmpp) (V)	41.4
MPP Current (Impp) (A)	9.91
Open Circuit Voltage (Voc) (V)	49.5
Short Circuit Current (Isc) (A)	10.55
No. of cells in series (Ns)	72

Figures 3.3 and 3.4 represent the I-V and the P-V curves for the model. This has been done in order to verify the model made. The MPPT Boost Converter has a PV string consisting of 18 of these panels connected in series at the input. Equations 2.12, 2.13 and 2.16-2.21 were used to make the model of this panel since the  $V_{oc}, I_{sc}, V_{mpp}, I_{mpp}, N_s$  is mentioned in the datasheet. The considered temperature is  $25^\circ C$ . Based on the equations and the specifications, the values have been calculated for a single panel have been shown in Table 3.2.

The converter circuit to which the PV string is connected has the following specifications: Table 3.3.

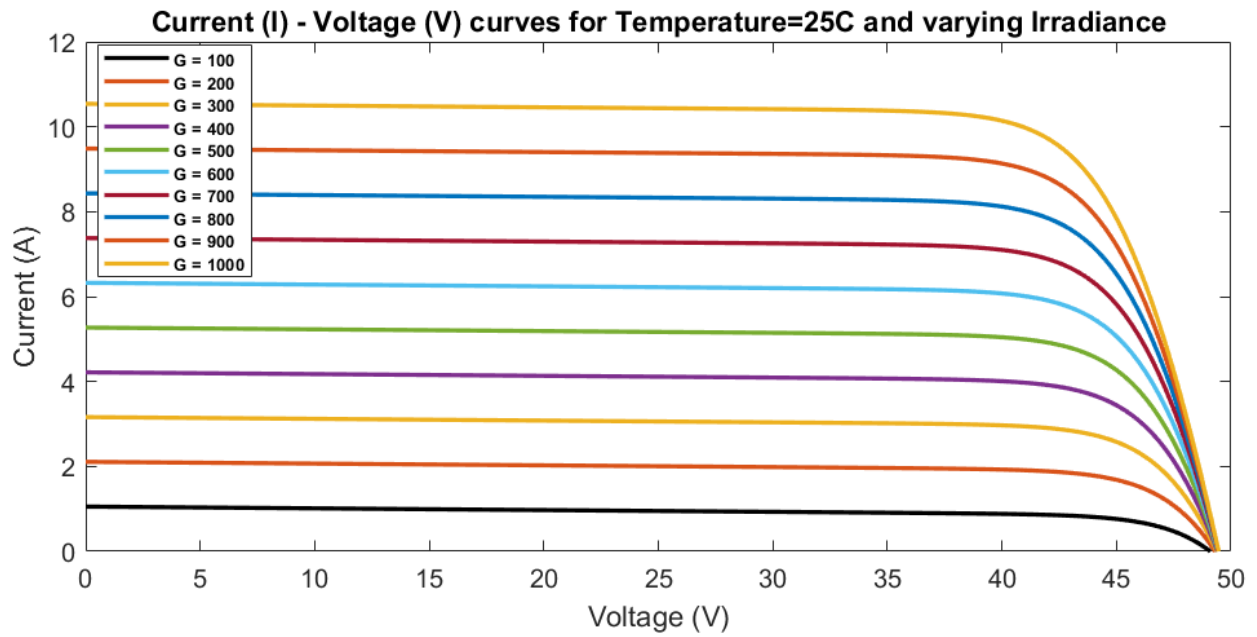


Figure 3.3: Current-Voltage curves for different irradiance levels based on the model created for the LG410N2W-L5 panel

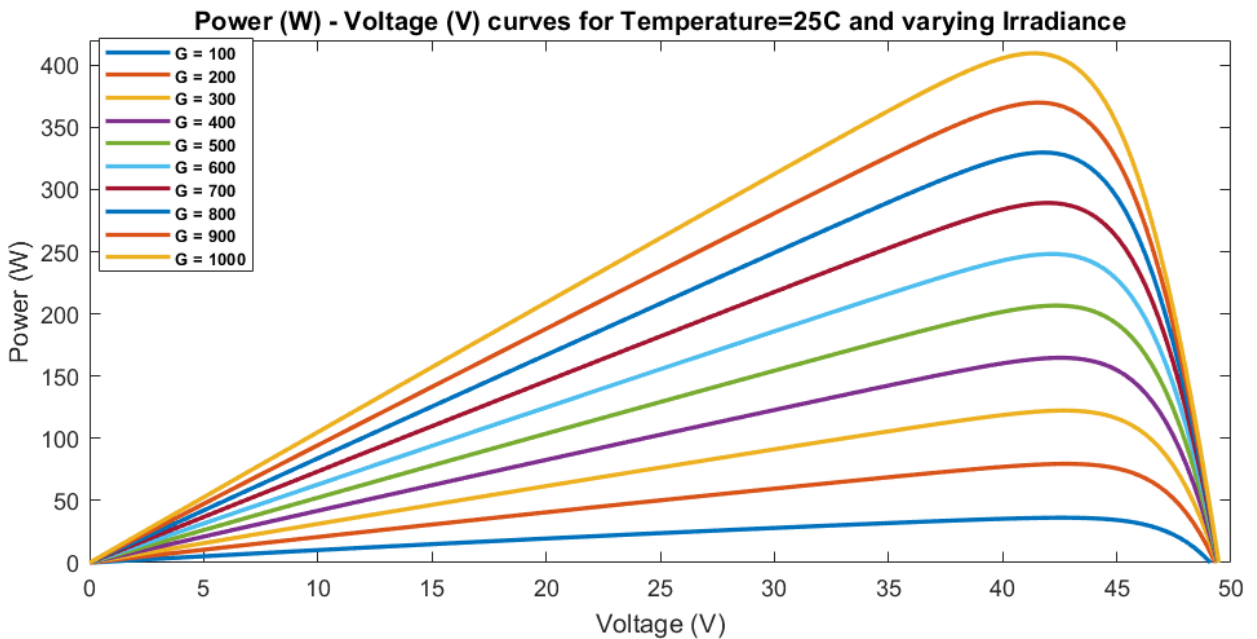


Figure 3.4: Power-Voltage curves for different irradiance levels based on the model created for the LG410N2W-L5 panel

After the model of the solar PV string is made, the required parameters from that are used in the model of the converter to make the final model and get the transfer functions for implementing the control. The Output parameters to Duty Cycle Transfer Functions are:

$$\frac{\tilde{i}_L(s)}{\tilde{d}(s)} = \frac{2.143 \times 10^6 s + 2.221 \times 10^8}{s^2 + 103.7s + 1.299 \times 10^9} \quad (3.15)$$

Table 3.2: Calculated PV Model parameters

Calculated Parameter	Value
Ideality Factor( $\eta$ )	1.0212
Saturation Current ( $I_{sat}$ )	$4.3936 \times 10^{-11}$
Series Resistance ( $R_s$ )	$0.2281\Omega$
Series Resistance ( $R_p$ )	$243.42\Omega$

Table 3.3: Specifications of the MPPT Boost Converter

Parameter	Value/Specification
Input Capacitor( $C_{in}$ )	$22\mu F$
Inductor ( $L$ )	$350\mu H$
Input Capacitor( $C_{out}$ )	$45.22\mu F$
Maximum Input Voltage ( $V_{in,max}$ )	$750V$
Maximum Input Current ( $I_{in,max}$ )	$10A$

$$\frac{v_{\tilde{c}_{in}}(s)}{\tilde{d}(s)} = \frac{-9.74 \times 10^{11}}{s^2 + 103.7s + 1.299 \times 10^9} \quad (3.16)$$

These transfer functions have been used to design the control for the converter.

### 3.2 MPPT Converter for a Bipolar DC Micorgrid

The circuit in Figure 3.5 is a DC-DC Boost Converter designed for a Bipolar DC Microgrid. Both the circuits in the current layout are independent from each other and each linked to a distinct PV string. This converter's output consists of three lines: positive, neutral, and negative. The output side is connected microgrid. The linearization of the diode resistance stands here as well making the model valid under

$$R_P = R_{sh} || R_d$$

. One MOSFET, two diodes, and two inductors are present for each circuit. Since both the circuits are independent from each other and have the identical model for the top and the bottom converter circuits. A subscript 'n' has been put for each parameter where n=1 and n=2 can be addressed for top and bottom section respectively. The same state, input and output parameters have been considered for this topology as well.

The State (x), Input (u) and the Output (y) parameters considered for modelling are:

$$x_n = \begin{pmatrix} i_{L_n} \\ v_{c_{inn}} \end{pmatrix} \quad u_n = \begin{pmatrix} i_{ph_n} \\ v_{out_n} \end{pmatrix} \quad y_n = \begin{pmatrix} i_{L_n} \\ v_{c_{inn}} \end{pmatrix} \quad (3.17)$$

For the ON TIME, using KVL and KCL, the State Equation and the Output Equation can be mentioned as

$$\begin{pmatrix} \dot{i}_{L_n} \\ \dot{v}_{c_{inn}} \end{pmatrix} = \begin{pmatrix} 0 & \frac{1}{L} \\ -1 & -1 \\ C_{inn} & R_{Pn}C_{inn}(1 + \frac{R_{Sn}}{R_{Pn}}) \end{pmatrix} \begin{pmatrix} i_{L_n} \\ v_{c_{inn}} \end{pmatrix} + \begin{pmatrix} 0 & 0 \\ 0 & 1 \\ 0 & C_{inn}(1 + \frac{R_{Sn}}{R_{Pn}}) \end{pmatrix} \begin{pmatrix} i_{ph_n} \\ v_{out_n} \end{pmatrix} \quad (3.18)$$

$$\begin{pmatrix} i_{L_n} \\ v_{c_{inn}} \end{pmatrix} = \begin{pmatrix} 1 & 0 \\ 0 & 1 \end{pmatrix} \begin{pmatrix} i_{L_n} \\ v_{c_{inn}} \end{pmatrix} + \begin{pmatrix} 0 & 0 \\ 0 & 0 \end{pmatrix} \begin{pmatrix} i_{ph_n} \\ v_{out_n} \end{pmatrix} \quad (3.19)$$

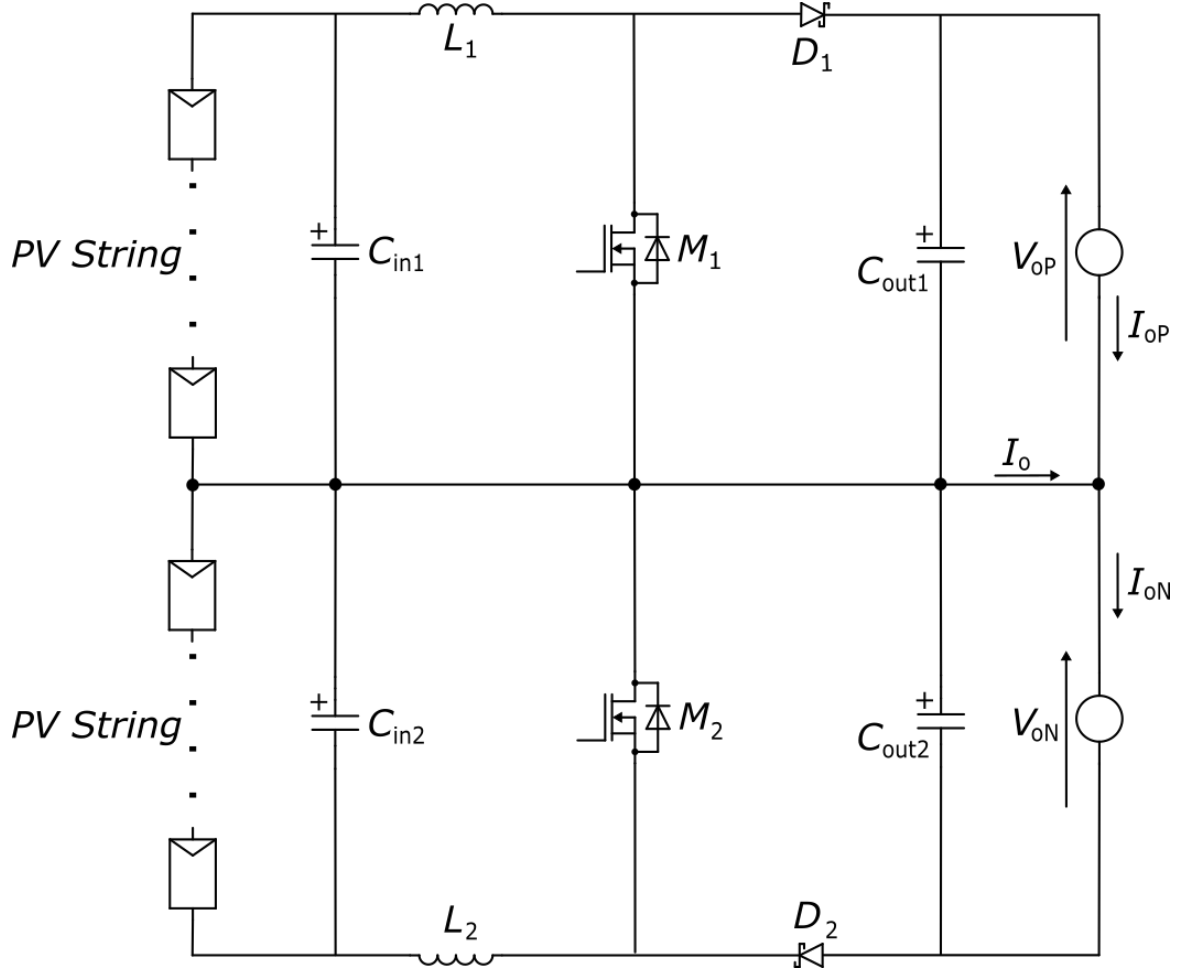


Figure 3.5: PV Powered Boost Converter for Bipolar DC Microgrids [34]

thus representing  $\dot{x} = A_1x + B_1u$  and  $y = C_1x + D_1u$  in their respective and accurate manner. For the OFF TIME, using KVL and KCL, the State Equation and the Output Equation can be mentioned as

$$\begin{pmatrix} \dot{i}_{L_n} \\ \dot{v}_{c_{inn}} \end{pmatrix} = \begin{pmatrix} 0 & \frac{1}{L} \\ -1 & \frac{-1}{R_{Pn}C_{inn}(1 + \frac{R_{Sn}}{R_{Pn}})} \end{pmatrix} \begin{pmatrix} i_{L_n} \\ v_{c_{inn}} \end{pmatrix} + \begin{pmatrix} \frac{-1}{L_n} & 0 \\ 0 & \frac{1}{C_{inn}(1 + \frac{R_{Sn}}{R_{Pn}})} \end{pmatrix} \begin{pmatrix} i_{ph_n} \\ v_{out_n} \end{pmatrix} \quad (3.20)$$

$$\begin{pmatrix} i_{L_n} \\ v_{c_{inn}} \end{pmatrix} = \begin{pmatrix} 1 & 0 \\ 0 & 1 \end{pmatrix} \begin{pmatrix} i_{L_n} \\ v_{c_{inn}} \end{pmatrix} + \begin{pmatrix} 0 & 0 \\ 0 & 0 \end{pmatrix} \begin{pmatrix} i_{ph_n} \\ v_{out_n} \end{pmatrix} \quad (3.21)$$

thus representing  $\dot{x} = A_2x + B_2u$  and  $y = C_2x + D_2u$  in their respective and accurate manner. Once this set of equations is obtained, the averaging procedure is performed by multiplying all the ON TIME matrices with duty cycle  $\mathbf{d}$  and the OFF TIME matrices are multiplied with  $\mathbf{1} - \mathbf{d}$  performing the averaging procedure, similar to the earlier section. Finally, the averaged matrices calculated are

$$A_{n_{avg}} = \begin{pmatrix} 0 & \frac{1}{L_n} \\ -1 & \frac{-1}{R_{Pn}C_{inn}(1 + \frac{R_{Sn}}{R_{Pn}})} \end{pmatrix} \quad B_{n_{avg}} = \begin{pmatrix} \frac{-(1-d_n)}{L_n} & 0 \\ 0 & \frac{1}{C_{inn}(1 + \frac{R_{Sn}}{R_{Pn}})} \end{pmatrix} \quad (3.22)$$

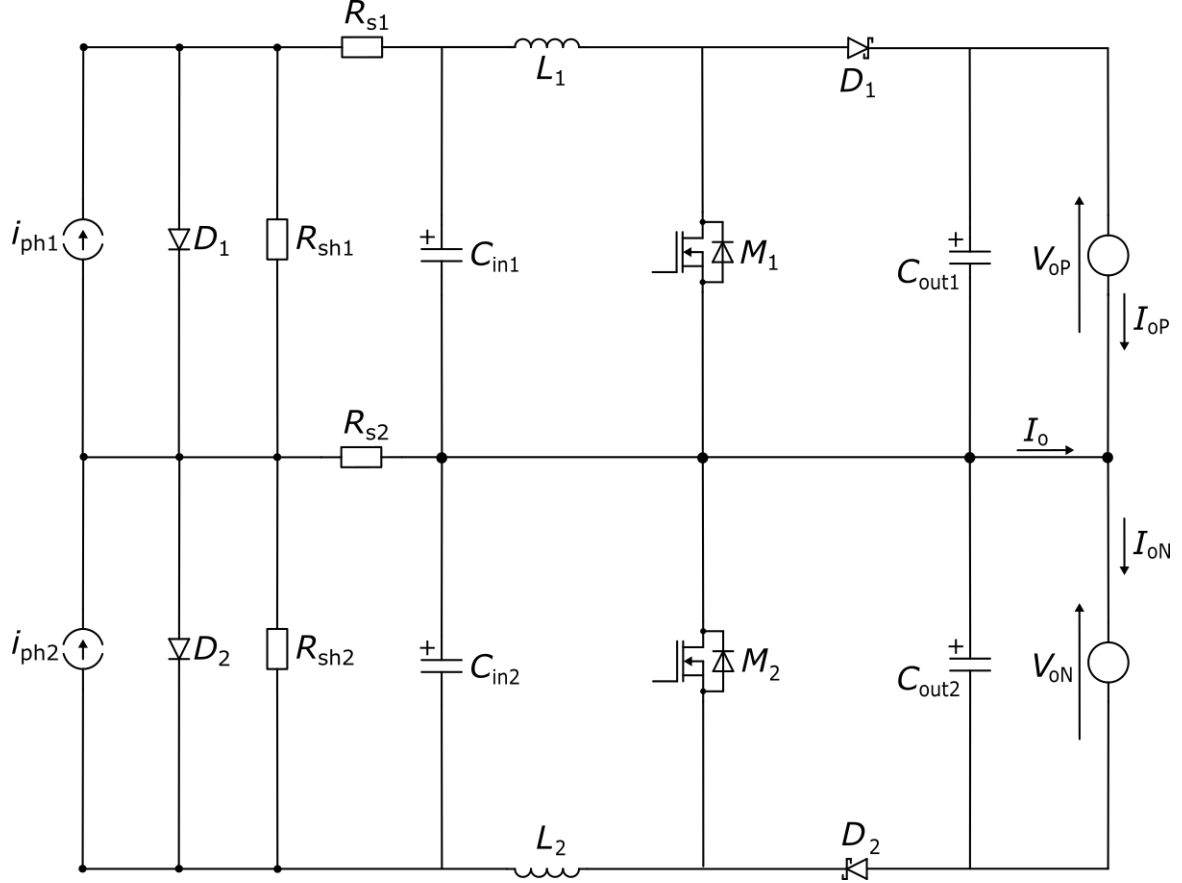


Figure 3.6: Grid connected Boost Converter for Bipolar DC Microgrids with PV model at its input

$$C_{n_{avg}} = \begin{pmatrix} 1 & 0 \\ 0 & 1 \end{pmatrix} \quad D_{n_{avg}} = \begin{pmatrix} 0 & 0 \\ 0 & 0 \end{pmatrix} \quad (3.23)$$

After the averaging procedure is complete, signal perturbations are added to all the state, input and output parameters and the duty cycle. The capital letters indicate the Steady State terms and the letters with tilde on them indicate the small signal perturbations, for example  $i_L = I_L + \tilde{i}_L$ .

$$x_n = \begin{pmatrix} I_{L_n} + \tilde{i}_{L_n} \\ V_{C_{inn}} + \tilde{v}_{C_{inn}} \end{pmatrix} \quad u_n = \begin{pmatrix} I_{ph_n} + \tilde{i}_{ph_n} \\ V_{o_n} + \tilde{v}_{o_n} \end{pmatrix} \quad y_n = \begin{pmatrix} I_{L_n} + \tilde{i}_{L_n} \\ V_{C_{inn}} + \tilde{v}_{C_{inn}} \end{pmatrix} \quad (3.24)$$

$$A_{n_{avg}} = \begin{pmatrix} 0 & \frac{1}{L_n} \\ -\frac{1}{C_{inn}} & -\frac{1}{R_{Pn}C_{inn}(1 + \frac{R_{Sn}}{R_{Pn}})} \end{pmatrix} \quad B_{n_{avg}} = \begin{pmatrix} \frac{-(1 - (D_n + \tilde{d}_n))}{L_n} & 0 \\ 0 & \frac{1}{C_{inn}(1 + \frac{R_{Sn}}{R_{Pn}})} \end{pmatrix} \quad (3.25)$$

$$C_{n_{avg}} = \begin{pmatrix} 1 & 0 \\ 0 & 1 \end{pmatrix} \quad D_{n_{avg}} = \begin{pmatrix} 0 & 0 \\ 0 & 0 \end{pmatrix} \quad (3.26)$$

After the addition of signal perturbations, the equations are written in the format as shown in equations 2.5 and 2.6, to calculate the Transfer Functions between the output and the input parameters.

### 3.2.1 Application in the project

This is used to power a bipolar DC Microgrid with PV as the input. The DC Microgrid has  $\pm 320V$  rated voltage. The converter circuit has the following specifications mentioned in Table ??.

Table 3.4: Specifications of the MPPT Converter for Bipolar DC Microgrid

Parameter	Value/Specification
Inductors( $L1, L2$ )	$200\mu H$
Input Capacitors( $C_{in1}, C_{in2}$ )	$50\mu F$
Output Capacitors( $C_{out1}, C_{out2}$ )	$90\mu F$
Maximum conversion power per input( $P$ )	$6kW$
Input voltage range ( $V_{in}$ )	$320V - 800V$
Maximum input current ( $I_{in}$ )	$10A$
Nominal output voltage per phase ( $V_{oP,nom}$ or $V_{oN,nom}$ )	$\pm 350V$
Output voltage range per phase( $V_{oP}$ or $V_{oN}$ )	$\pm 320V - \pm 400V$
Bipolar output voltage range( $V_o$ )	$640V - 800V$
Maximum output current per phase( $I_{oP}$ or $I_{oN}$ )	$18.5A$
Duty Cycle( $D$ )	$0 - 100\%$
Switching Frequency ( $f_s$ )	$75kHz$

The output to duty cycle transfer functions used to design the cascaded control loop are as follows:

$$\frac{i_{L_n}^{\sim}(s)}{\tilde{d}(s)} = \frac{2.143 \times 10^6 s + 1.318 \times 10^{10}}{s^2 + 6150s + 1.299 \times 10^9} \quad (3.27)$$

$$\frac{v_{c_{in}}^{\sim}(s)}{\tilde{d}(s)} = \frac{-9.74 \times 10^{11}}{s^2 + 6150s + 1.299 \times 10^9} \quad (3.28)$$

## 3.3 Implementation of Control

### MPPT and Droop Control

The Perturb and Observe MPPT algorithm has been implemented on both the converters. Usually, a simple P&O Algorithm senses the PV string's operating voltage and current to calculate the difference in power which is compared to the preceding power value. Finally at the output usually a variation in duty cycle is generated. This process makes the control of the converter a bit simple, but not robust for sudden variations in the operating conditions. DC-Opportunities has developed a P&O with adaptive step size. The step amplitude is calculated using the equation,

$$V_{n+1} = V_n \pm StepFactor \times \left( \frac{P_n - P_{n-1}}{V_n - V_{n-1}} \right) \quad (3.29)$$

The *StepFactor* here is defined based on the operating frequency of the algorithm. After the step is calculated, it is then summed with the voltage at the operating point i.e.  $V_n$ . The generated voltage set point is then provided to the cascaded PI controller. In this manner, the control over this converter becomes more robust than the basic method of P&O algorithm. Alongside the MPPT, Droop control has also been implemented. The Current-Voltage (I-V) type of Droop control strategy is implemented on the converters. When multiple converters are connected in parallel to a grid, every converter's output voltage will not be as constant always. The converters with higher output voltage will generate higher power. The converter's generated power is compared with the power requirement of the grid and depending on that the output current is limited to a certain level depending on the output voltage of the grid. PLECS has been used to carry out the simulations and the algorithm and

the controllers have been put in PLECS for the same. A State machine has also been implemented which switches between Droop and MPPT control in case the grid voltage shoots up. The following subsection elaborates on the functioning of State Machine.

### Internal Control

For these boost converter circuits, the P&O MPPT algorithm with a cascaded PI control has been designed. The P&O algorithm senses the PV generated voltage and current values to calculate the input power. Depending on the power generated, a step factor is calculated in order to reach the MPP. This step factor has upper and lower limits so that the step is not very small or very large. Followed by the calculations, the step is then added to the input voltage. In this manner, the Perturb and Observe MPPT works to reach the maximum power point. This voltage is given as the set point to the cascaded PI controller. The design of the cascaded control and its operation will be discussed further in the section.

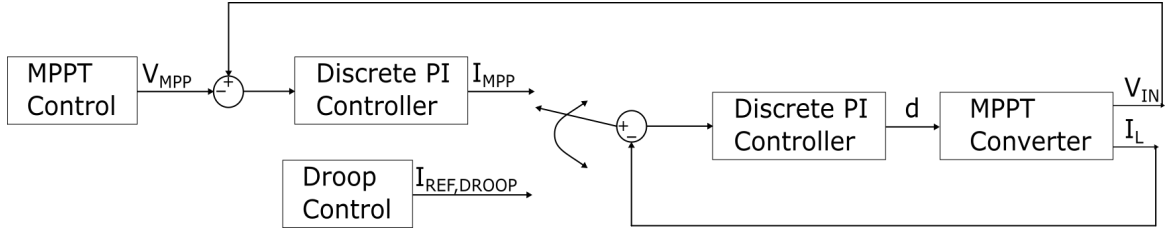


Figure 3.7: Cascade PI Control for the PV powered grid connected Boost Converter

Figure 3.7 shows the cascaded PI controller designed specifically for the Boost Converter. A cascade PI Controller has an inner loop where one of the output parameters of the converter's model is compared with the set point. The set point is provided by another PI controller, which performs a similar comparison action with a set point it receives. For this converter, the reference voltage has been generated from the MPPT algorithm, and that is initially compared with the actual input voltage at that time. The PI controller receives the error signal and later generates the correction signal to get a set point for the input current. This set point for input current is compared with actual input current and the PI controller in the inner loop generates the correction signal. That correction signal is sent to the converter circuit in the form of duty cycle. In this manner the designed cascaded PI controller works for this converter. Droop control has also been implemented on this converter circuit so that when the grid voltage fluctuates, the output current is limited. The inner loop is the only loop that functions during the droop control giving the set point of the current depending on the requirement.

The PI controller has a transfer function

$$G_{controller}(s) = K_P + \frac{K_I}{s} \quad (3.30)$$

The controller transfer function is multiplied with the plant's transfer function and finally can be written as

$$G_{Closed-Loop} = \frac{G_{controller}(s) \times G_{plant}(s)}{1 + G_{controller}(s) \times G_{plant}(s)} \quad (3.31)$$

#### 3.3.1 Boost Converter for tram lines

For the grid connected Boost Converter shown in Figure 3.1, this same approach was used to design the cascaded control loop. The transfer function from the inner loop is the inductor current ( $i_L$ ) to duty cycle ( $d$ ), which is given by,

$$\frac{i_{L_n}^{\sim}(s)}{\tilde{d}(s)} = \frac{2.143 \times 10^6 s + 1.318 \times 10^{10}}{s^2 + 6150s + 1.299 \times 10^9} \quad (3.32)$$

Since a discrete PI controller is used in this case, the transfer functions should also be in the discrete domain. The continuous-time and discretized systems are most closely matched in the frequency domain by the Tustin or bilinear approximation, which is done in MATLAB. In this process both, the open loop transfer function of the plant and the controller transfer function have been discretized separately. Later, they are multiplied to get the discrete closed loop transfer function. The sampling frequency for the inner part of the cascaded control loop is  $f_s = 2500Hz$ .

$$G_{Inner-Open-Loop,Discrete} \rightarrow \frac{\tilde{i}_L(z)}{\tilde{d}(z)} = \frac{17.64z^2 + 19.46z + 1.819}{z^2 + 1.881z + 0.9546} \quad (3.33)$$

After the Open Loop Transfer Function was verified through the step response, the controller transfer function was integrated to it as shown below.

$$G_{Controller,Discrete} = \frac{0.3776z - 0.148}{z - 1} \quad (3.34)$$

The Equation 3.34 is integrated with the transfer function stated in Equation 3.33 using the formula in subsection 3.3.

$$G_{Inner-Closed-Loop,Discrete} = \frac{6.66z^3 + 4.736z^2 - 2.194z - 0.2692}{7.66z^3 + 5.617z^2 - 3.12z - 1.224} \quad (3.35)$$

Figure 3.8 shows the unit step response for the closed loop transfer function in Equation 3.35 which

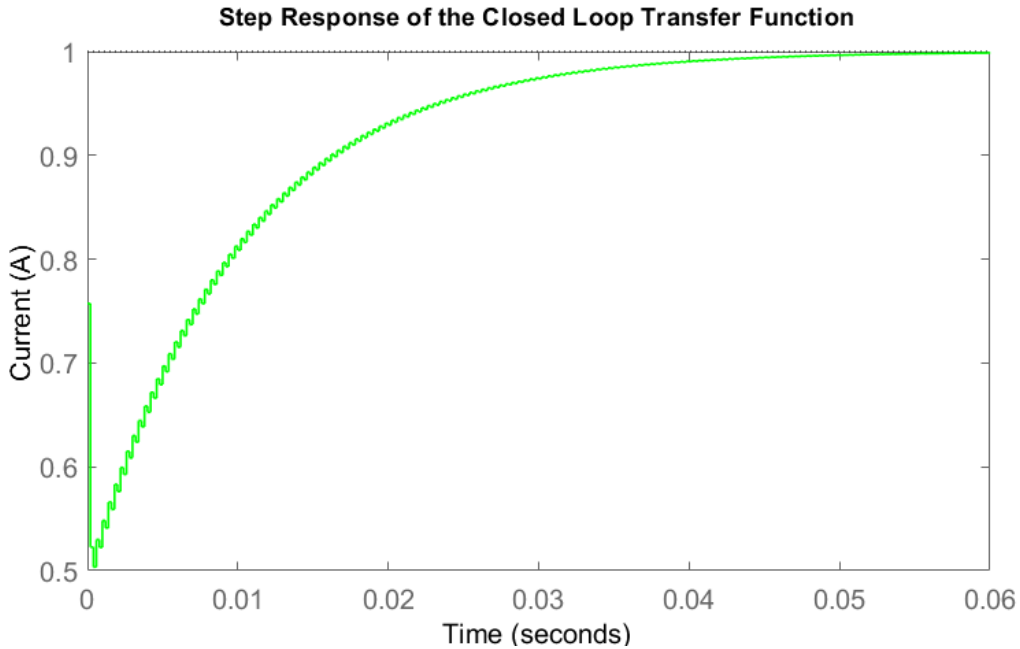


Figure 3.8: Closed loop Step Response of Equation 3.35

is the discretized closed loop transfer function for the inner part of the cascaded control loop. As seen here, when the controller transfer function i.e. Equation 3.34 is integrated with the open loop transfer function in Equation 3.33, the unit step response goes from zero to one as observed in Figure 3.8. This indicates that the closed loop transfer function reacts to the unit step input and reaches the steady state.

Once the closed loop transfer function for the inner part is generated, the same process is performed for the outer part of the cascaded control loop.

$$G_{Outer-Open-Loop} \rightarrow \frac{v_{\tilde{C}_{in}}(s)}{\tilde{d}(s)} = \frac{-9.74 \times 10^{11}}{s^2 + 6150s + 1.299 \times 10^9} \quad (3.36)$$

The above transfer function in Equation 3.36 is discretized using the same method as used for the inner part of the cascaded loop.

$$G_{Outer-Open-Loop,Discrete} = \frac{-719.1z^2 - 1438z - 719.1}{z^2 + 1.881z + 0.9546} \quad (3.37)$$

The equation 3.38 is the final open loop transfer function which is the product of the closed loop transfer function of the inner part and discrete open loop transfer function of the outer part.

$$G_{Complete-Open-Loop,Discrete} = \frac{-4790z^5 - 1.299e04z^4 - 1.002e04z^3 - 57.44z^2 + 1965z + 193.6}{7.66z^5 + 20.02z^4 + 14.76z^3 - 1.729z^2 - 5.28z - 1.168} \quad (3.38)$$

$$G_{Controller,Discrete} = \frac{-3.16 \times 10^{-5}z + 2.494 \times 10^{-5}}{z - 1} \quad (3.39)$$

The process of generating a closed loop transfer function of the complete cascaded loop uses the identical formula from subsection 3.3.

$$G_{Complete-Closed-Loop,Discrete} = \frac{0.1514z^6 + 0.2909z^5 - 0.007093z^4}{7.812z^6 + 12.65z^5 - 5.274z^4} \cdot \frac{-0.2482z^3 - 0.06351z^2 + 0.04288z + 0.004828}{-16.73z^3 - 3.614z^2 + 4.154z + 1.173} \quad (3.40)$$

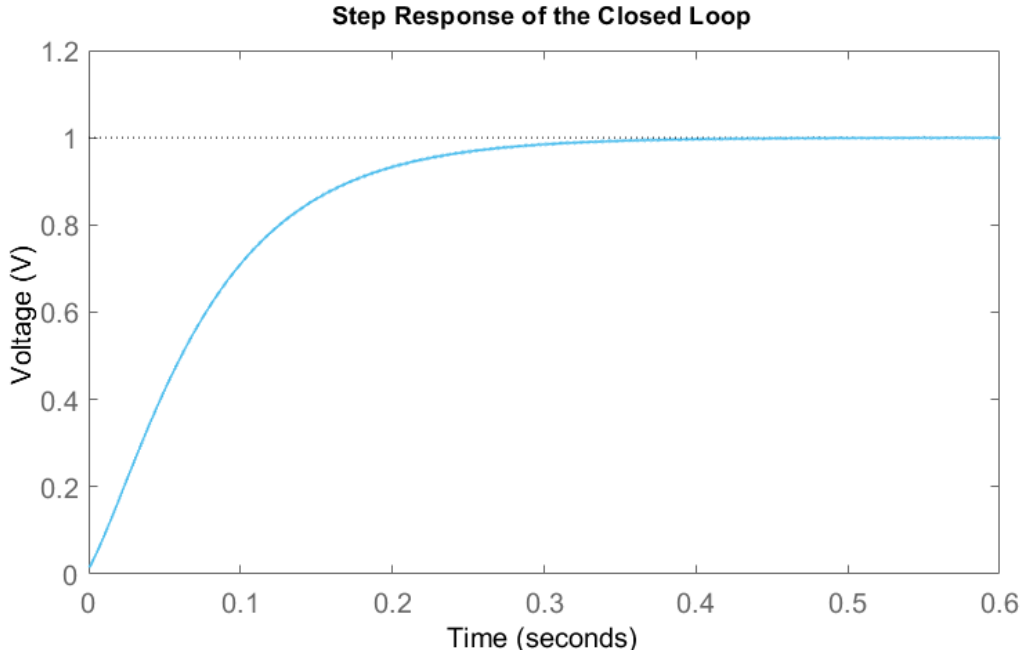


Figure 3.9: Closed loop Step Response of the Equation 3.40

After the integration of controller transfer function in Equation 3.39 with the open loop transfer function of the complete cascaded control loop shown in 3.38, the a unit step response it taken. Due to the presence of controller, the system is of a closed loop type and it thus settles to one as seen in Figure 3.40.

### 3.3.2 MPPT Converter for a Bipolar DC Micorgrid

This subsection elaborates more on the control strategy for the MPPT converter for DC Microgrids shown in Figure 3.6. Here 4 panels are connected in series at the input of each side. The cascaded control loop shown in Figure 3.7 was implemented on this converter and an identical approach was used for the internal controller. Since both the converters in Figure 3.6 are identical and independent, the control loop is designed for one and replicated for the other. The transfer functions for the cascaded control loop are as follows.

$$G_{Inner-Open-Loop} \rightarrow \frac{i_{L_n}^{\sim}(s)}{\tilde{d}(s)} = \frac{1.6 \times 10^6 s + 3.104 \times 10^7}{s^2 + 19.4s + 1 \times 10^8} \quad (3.41)$$

$$G_{Inner-Open-Loop,Discrete} \rightarrow \frac{i_{L_n}^{\sim}(z)}{\tilde{d}_n(z)} = \frac{64.2z^2 + 0.4963z - 63.7}{z^2 + 1.199z + 0.9984} \quad (3.42)$$

The controller transfer function was incorporated to the open loop transfer function after the step response was used to verify it.

$$G_{Controller,Discrete} = \frac{0.52z - 0.48}{z - 1} \quad (3.43)$$

The controller transfer function is integrated with the open loop transfer function to obtain the closed loop transfer function.

$$G_{Inner-Closed-Loop,Discrete} = \frac{33.38z^3 - 30.56z^2 - 33.36z + 30.58}{34.38z^3 - 30.36z^2 - 33.56z + 29.58} \quad (3.44)$$

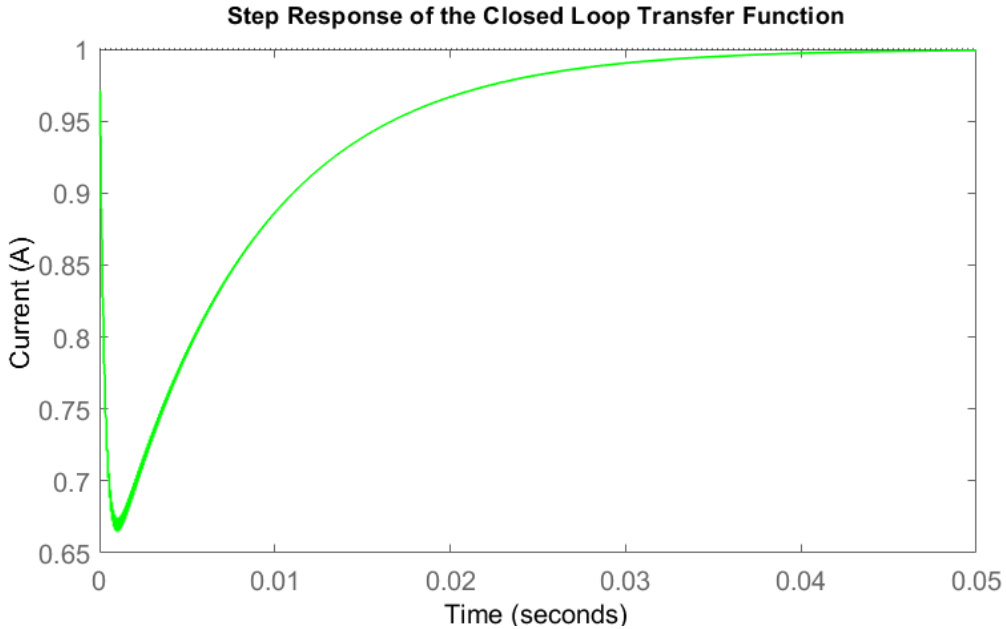


Figure 3.10: Closed loop Step Response of Equation 3.44

Figure 3.10 shows the unit step response for the closed loop transfer function in Equation 3.44 which is the discretized closed loop transfer function for the inner part of the cascaded control loop. Since the step response goes to one, the presence of the controller is validated.

Now, identical process is performed for the outer part of the cascaded control loop which gives the following transfer functions.

$$G_{Outer-Open-Loop} \rightarrow \frac{v_{\tilde{C}_{inn}}(s)}{\tilde{d}_n(s)} = \frac{-3.2 \times 10^{10}}{s^2 + 19.4s + 1 \times 10^8} \quad (3.45)$$

$$G_{Outer-Open-Loop,Discrete} \rightarrow \frac{v_{\tilde{C}_{inn}}(z)}{\tilde{d}_n(z)} = \frac{-255.7z^2 - 511.4z - 255.7}{z^2 + 1.199z + 0.9978} \quad (3.46)$$

$$G_{Complete-OpenLoop,Discrete} = \frac{-8539z^5 - 9262z^4 + 1.563e04z^3 + 1.706e04z^2 - 7109z - 7822}{34.38z^5 + 10.87z^4 - 35.64z^3 - 40.98z^2 + 1.955z + 29.53} \quad (3.47)$$

$$G_{Controller,Discrete} = \frac{-2 \times 10^{-5}z}{z - 1} \quad (3.48)$$

$$G_{Complete-ClosedLoop} = \frac{0.1708z^6 + 0.1852z^5 - 0.3126z^4 - 0.3413z^3}{34.55z^6 - 23.33z^5 - 46.82z^4 - 5.684z^3} \frac{+0.1422z^2 + 0.1564z}{+43.08z^2 + 27.73z - 29.53} \quad (3.49)$$

After the integration of the controller transfer function shown in Equation 3.48 with the open loop

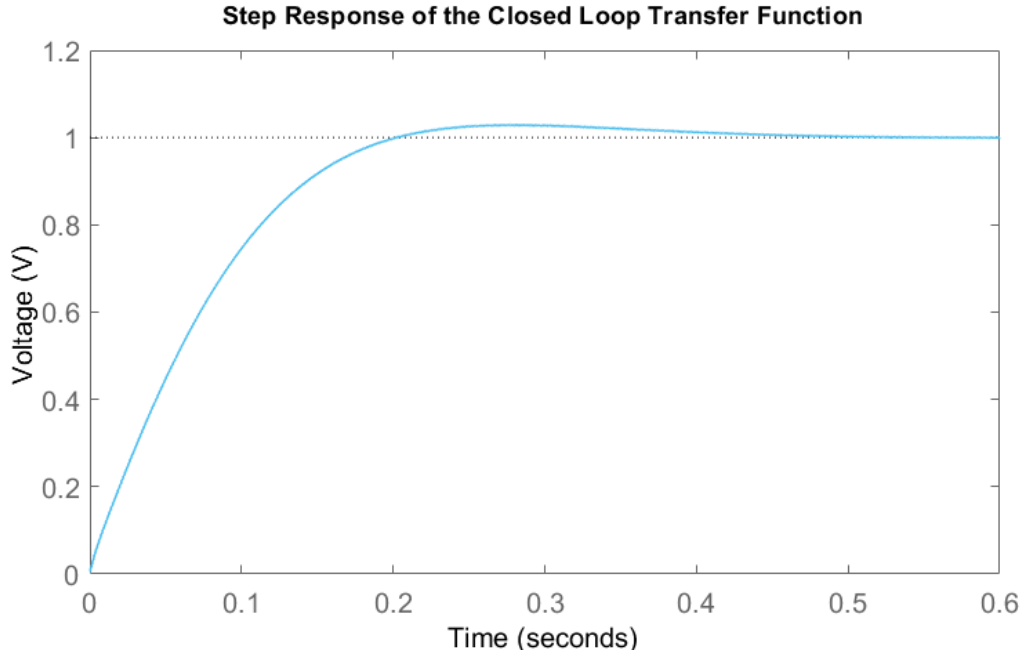


Figure 3.11: Closed loop Step Response of Equation 3.49

transfer function of the complete cascaded loop shown in Equation 3.47, the step response of the complete cascaded control loop settles at one due to the presence of the controller in both the loops, which can be observed in Figure3.11.

### 3.4 C-Script and State Machine

PLECS uses C-script as a mean to implement customized control loops/algorithms using C programming language. It contributes in interaction with the solver engine on a similar level as the built in blocks. No manual compilation of any code is required, not even the installation of a compiler. The C code is instantly converted to native machine code via a built-in compiler, and it is then dynamically

linked into PLECS. The P&O MPPT algorithm and the Droop algorithm have been implemented using C-script. Along with these algorithms, a State Machine has also been implemented. The state machine has the C-script embedded into it.

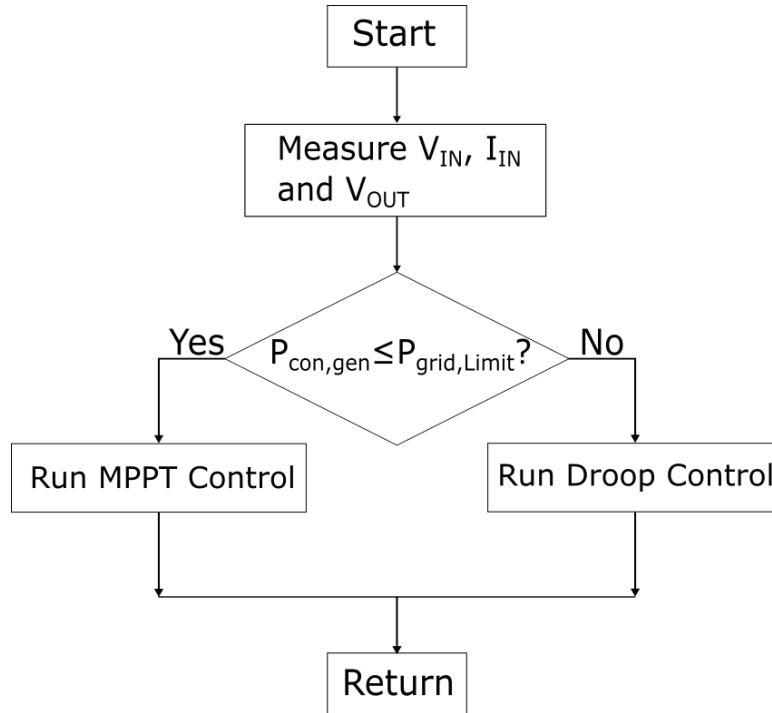


Figure 3.12: State Machine function flowchart

Figure 3.12 shows the flowchart for the function of the state machine. The state machine receives the inputs  $V_{in}$ ,  $I_{in}$ ,  $V_{out}$  i.e. input voltage, input current and the output voltage. Depending on the received inputs, the state machine defines whether to run the MPPT or the droop control. Once the state is defined, the code for the respective control is run to implement the control on the converter. The slope for the droop control is also calculated in the state machine itself. The flow of the control is described as follows. Depending on the operating conditions, the State machine selects whether to enter the Droop mode or MPPT mode. If the converter enters the MPPT mode of operation, then the Perturb & Observe MPPT algorithm extracts the input voltage and current to calculate the maximum power point and thus generates a set point for the maximum power point voltage. The internal controller then gives the set point for current which is sent in the form of duty cycle to the switch. In this manner, the converter operates around the MPP point depending on the operational conditions. In case the Droop control is activated, then the internal controller gets the set point for the current and thus the converter operates on the droop slope characteristic till the time when the voltage at the output side is regulated and the state is switched back to MPPT. After the control loop design was complete, this control flow was implemented in simulations in order to make sure that the control functions on the converters. This was followed by implementing the strategy on the hardware for testing the performance.

## 4.1 Boost Converter for tram lines

### 4.1.1 Simulation Results

The simulation of this circuit was carried out in PLECS. The following operating conditions are considered here. The panels have an open circuit voltage of  $V_{oc} = 49.5V$  and a short circuit current of  $I_{sc} = 10.55A$  and Maximum power point voltage  $V_{mpp} = 41.4V$  and current of  $I_{mpp} = 9.91$ . Here, 18 PV panels are connected in series at the input which makes maximum power voltage  $V_{mpp,input} = 745V$  and maximum power point current  $I_{mpp,input} = 9.91$ . The output side voltage has been set to  $V_{out} = 800V$ . When the operation is started, the irradiance is set to  $G = 1000W/m^2$ . The irradiance has been changed over the time in the form of steps to observe its effect on the control. The steps have been kept random to examine whether the control designed is robust enough to perform well under sudden changes in irradiance. The switching frequency has been kept at 50kHz. The P&O MPPT algorithm runs at 20Hz frequency and the step factor has been set to 1 in order to keep a small step size.

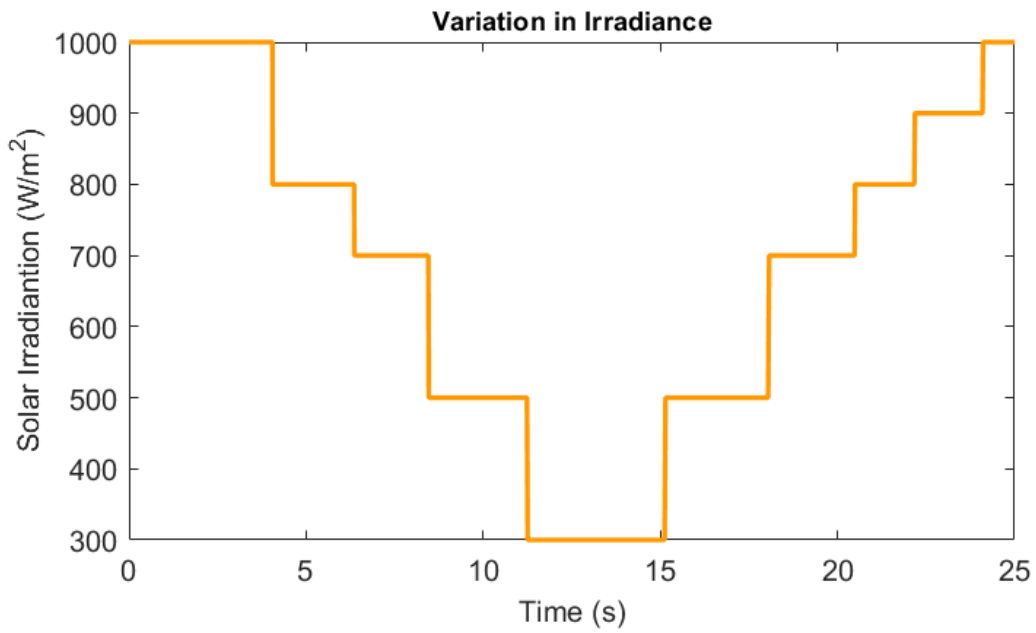


Figure 4.1: Variation in Irradiance during the operation in MPPT

Initially the Irradiance is set at  $1000W/m^2$ . MPPT algorithm kicks in, and thus gives the set point to the controller in the form of steps. At 2.5 seconds the control reaches the maximum power point value for the mentioned irradiance value. At approximately 4 seconds, the irradiance is reduced to  $G = 800W/m^2$  as observed in Figure 4.1.

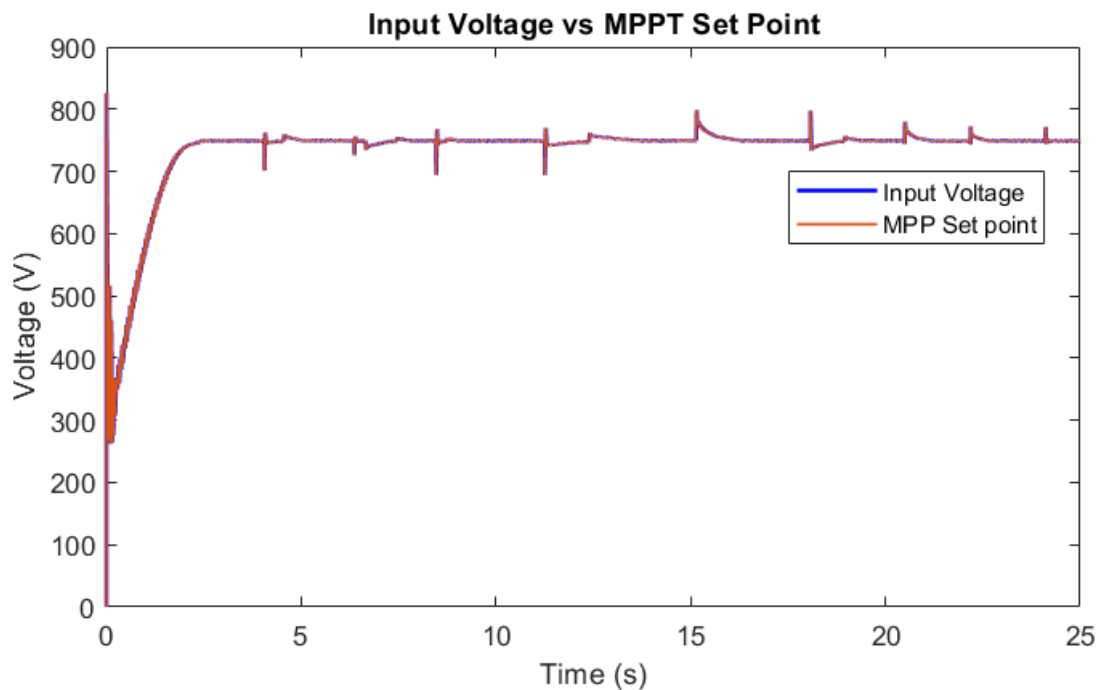


Figure 4.2: Input Voltage vs Set Point under MPPT Operation

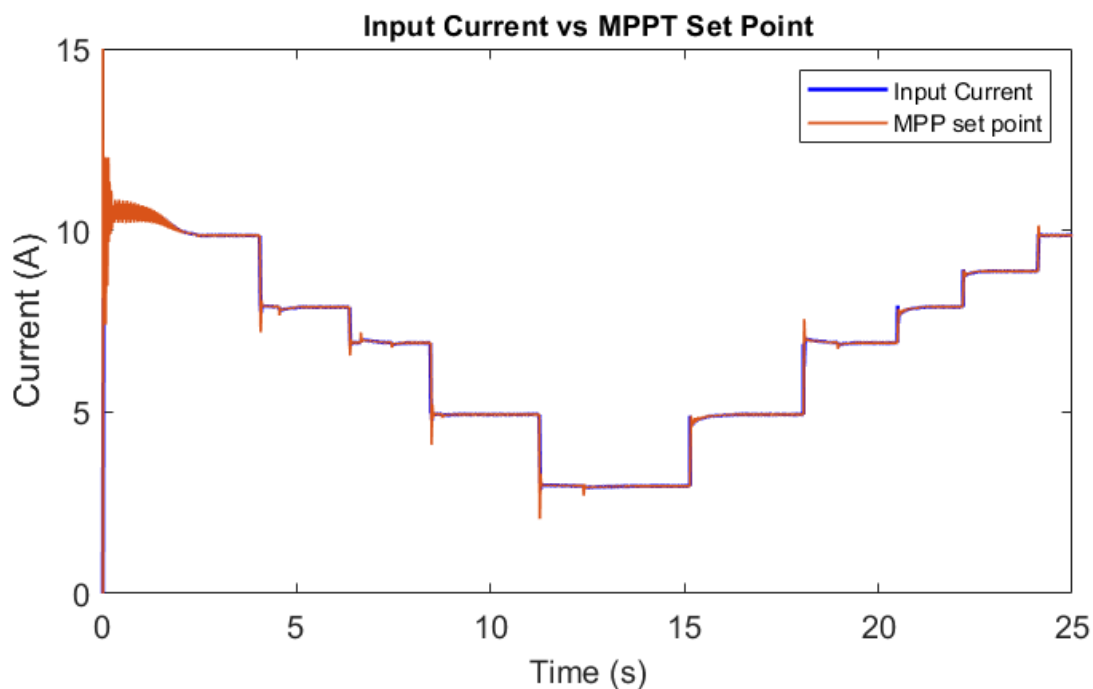


Figure 4.3: Input current vs Set Point under MPPT Operation

Due to the reduction in irradiance, the PV generator now produces lesser current i.e. 8A and that is supplied as the set point for the current controller (inner part of the cascaded control loop). The behaviour of current can be seen as shown in Figure 4.3. The voltage controller (outer part of the cascaded control loop) runs at 250Hz which is 10 times slower than the current controller. When the input current reduces, the current controller produces a higher duty cycle to supply the value to the output side. The lower frequency of the voltage controller thus the feedback process takes times the error thus builds up and when the feedback process is complete i.e. after the completion of 0.004 seconds unlike the current controller of which the feedback process is done at 0.0004 seconds, the input voltage reduces initially, but quickly recovers back to the correct value. At 3.8 seconds, irradiance is reduced to  $G = 700W/m^2$  which again results into reduction in the current. The internal PI controller gives the required set points and the input control is complete.

Table 4.1: Variation in the input current depending on the variation in Irradiance

Irradiance ( $W/m^2$ )	Input Current (A)
1000	9.8
800	7.8
700	6.9
500	4.9
300	3
500	5
700	7
800	7.9
900	8.9
1000	9.8

The above table shows the values for input current variations with respect to the change in irradiance under MPPT mode of operation.

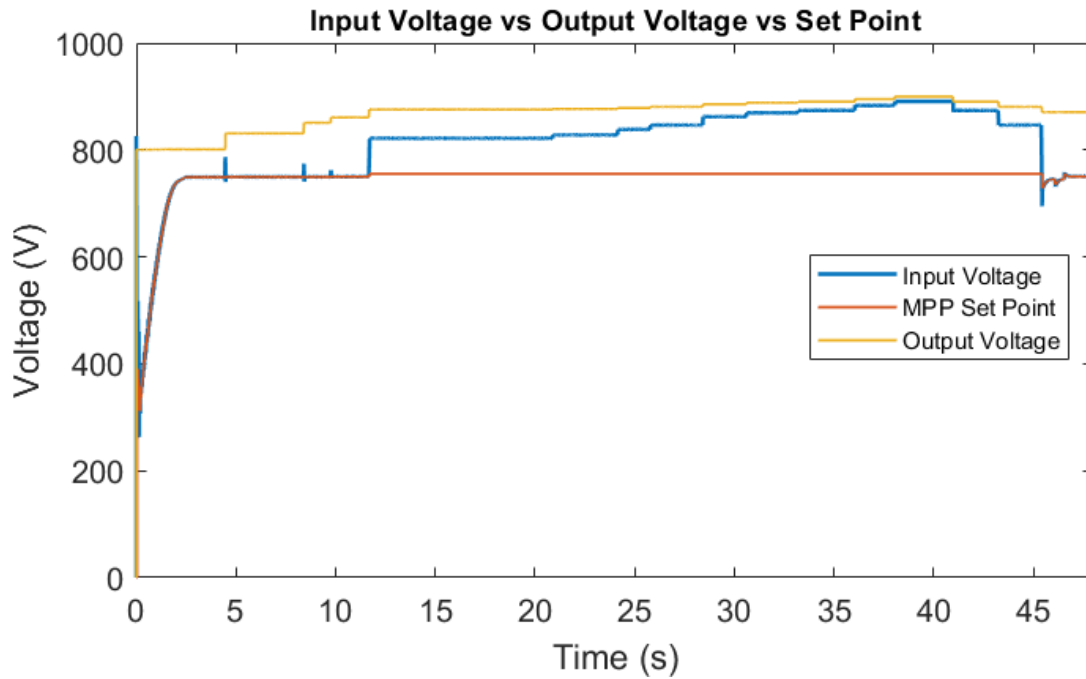


Figure 4.4: Voltage measurements during MPPT and Droop mode switching

Figures 4.4, 4.5 show the performance when the operation is changed between MPPT to Droop mode. At approximately 8 seconds, the grid voltage increases to 850V and the state machine switches from MPPT to Droop mode. After the state is switched, the control recovers and the inner part of the cascaded control loop is thus activated. Thus the current set point is given and the input current follows it.

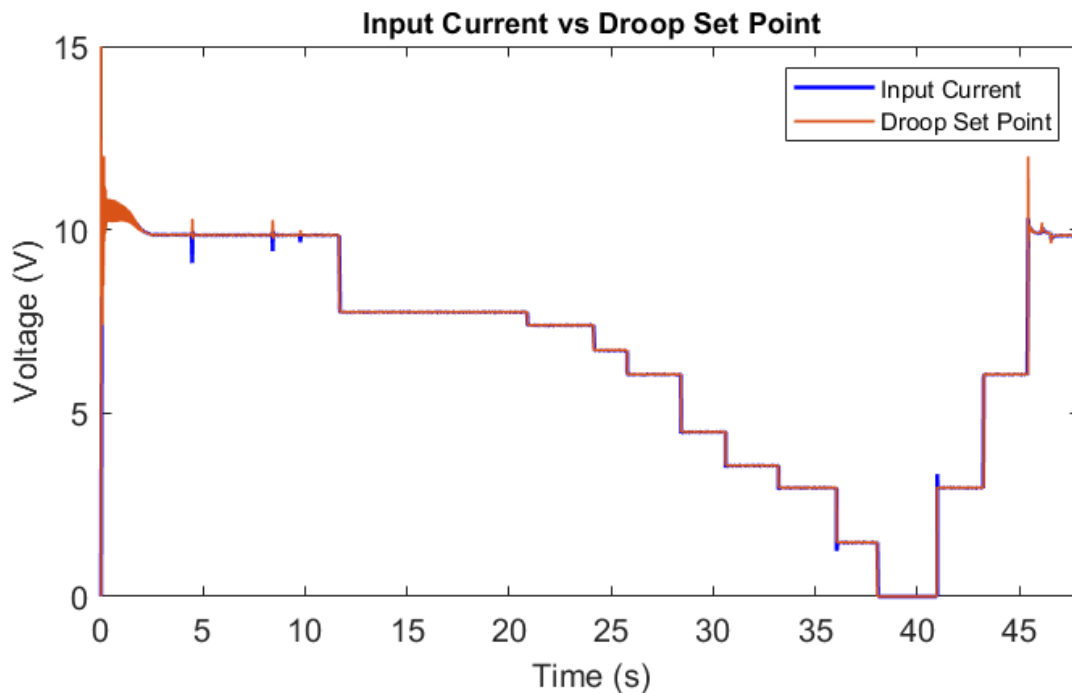


Figure 4.5: Current measurements during MPPT and Droop mode switching

Figure 4.4 shows the graph for the voltages when the state is switched from MPPT to Droop operation. Initially the converter operates in MPPT mode and at 11 seconds, the output side voltage

is increased to 875V in stages from 800V and the state switches from MPPT to Droop mode. In Figure 4.5 the behaviour of the current can be observed when MPPT to Droop transition is performed. When Droop mode is activated, the inner loop receives the current set point based on the voltage at the output side. When the voltage increases to 900V from 875V, the converter output current is limited in order to operate the converter on the droop characteristics. At 900V output voltage the input current is limited to 0A. After the output side voltage is reduced back to 870V, the state is switched to MPPT and the converter thus operates in MPPT mode.

#### 4.1.2 Hardware Results

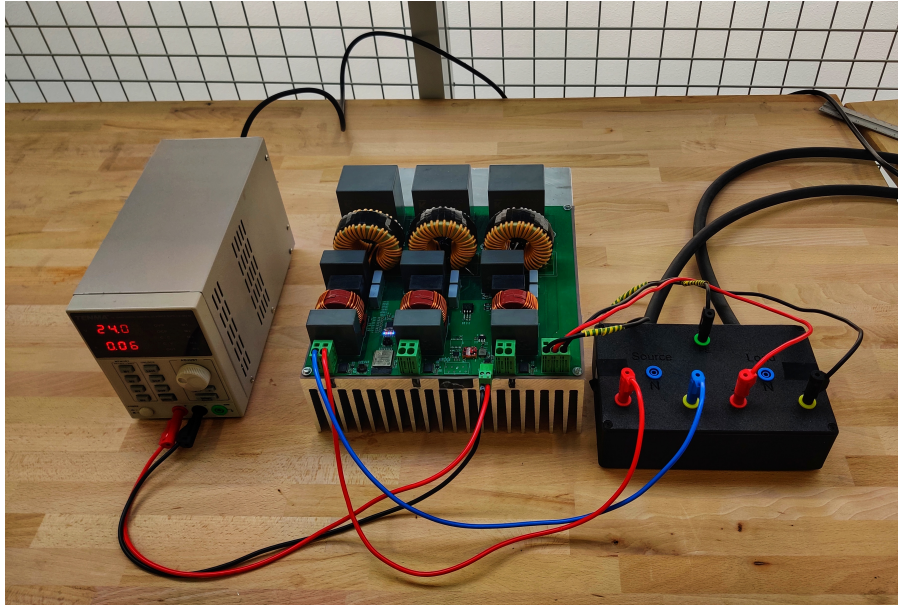


Figure 4.6: Hardware of the Boost Converter

The Hardware connections is shown in Figures 4.6 and 4.7. Figure 4.6, shows the Boost converter with the power supply on the left side and the power connection box on the right. The power connection block is connected to the source and the load through the black cables. The left side of the PCB has been connected to the left side of the black box which is the source side and the right side of the PCB connected to right side of the box is the load side. The source and the load have been simulated using the cabinets shown in Figure 4.7. The Delta supplies have a feature of the PV simulator. Users can enter the open circuit and the maximum power point values of the panel/string. Along with that the salient features of variation in irradiance and temperature are also present. The grid voltage has been set to approximately  $V_{out} = 720V$ , input is set around  $V_{in} = 400V$ . Then the test was commenced.

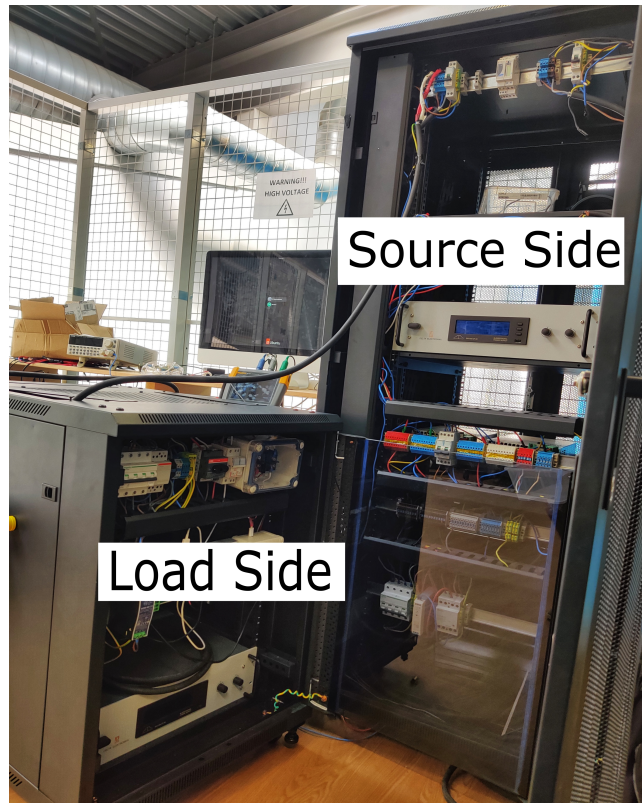


Figure 4.7: Source and Load side

Figure 4.7, shows the source and the load side. The Delta supply in the tall cabinet in the right side, is the source which simulates the behaviour of PV. The Delta supply in the small cabinet is the load side which simulates the behaviour of the grid. The PCB has been powered up with a 24V power supply for the functioning of the basic power circuitry and microcontroller unit. Followed by this, the connections to the input i.e. PV simulator and the output i.e. Grid simulated by the Delta supply have been made.

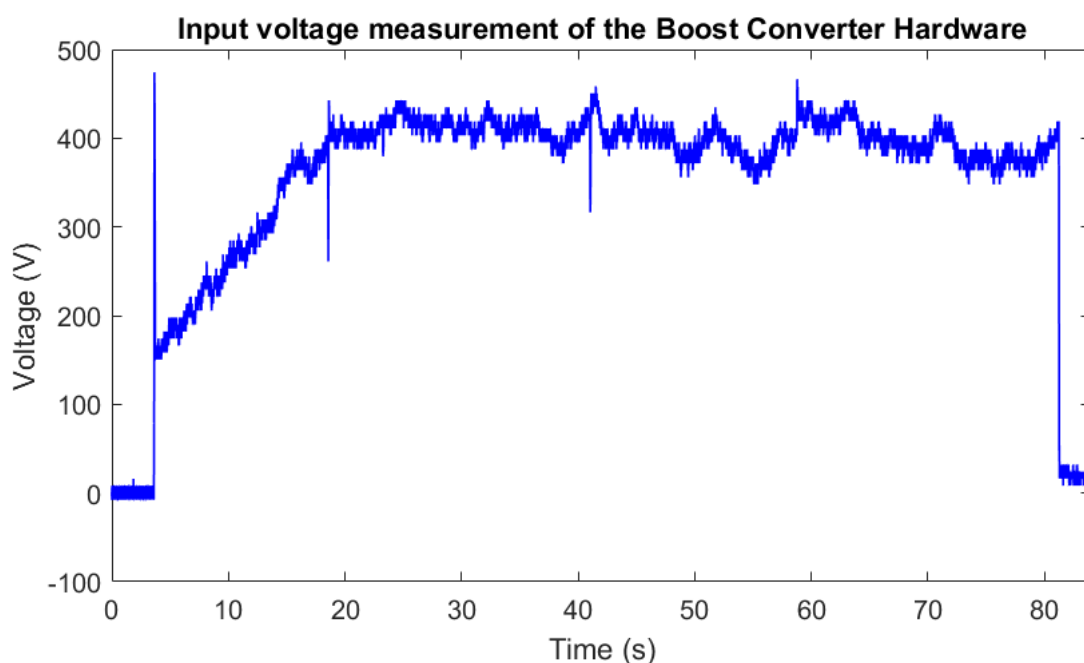


Figure 4.8: Input Voltage of the Boost Converter Hardware during MPPT operation

The Hardware test was begun with an irradiance of  $G = 1000W/m^2$  with input voltage set to  $V_{in} = 400V$  and the output side was simulated as a grid, thus keeping the voltage at approximately  $V_{out} = 720V$ . The irradiance was varied from  $G = 1000W/m^2$  to  $G = 600W/m^2$  to  $G = 200W/m^2$  and finally to  $G = 700W/m^2$ . The input voltage follows the MPP set point and thus increases to 400V in approximately 20 seconds which is considerably higher than the simulation results.

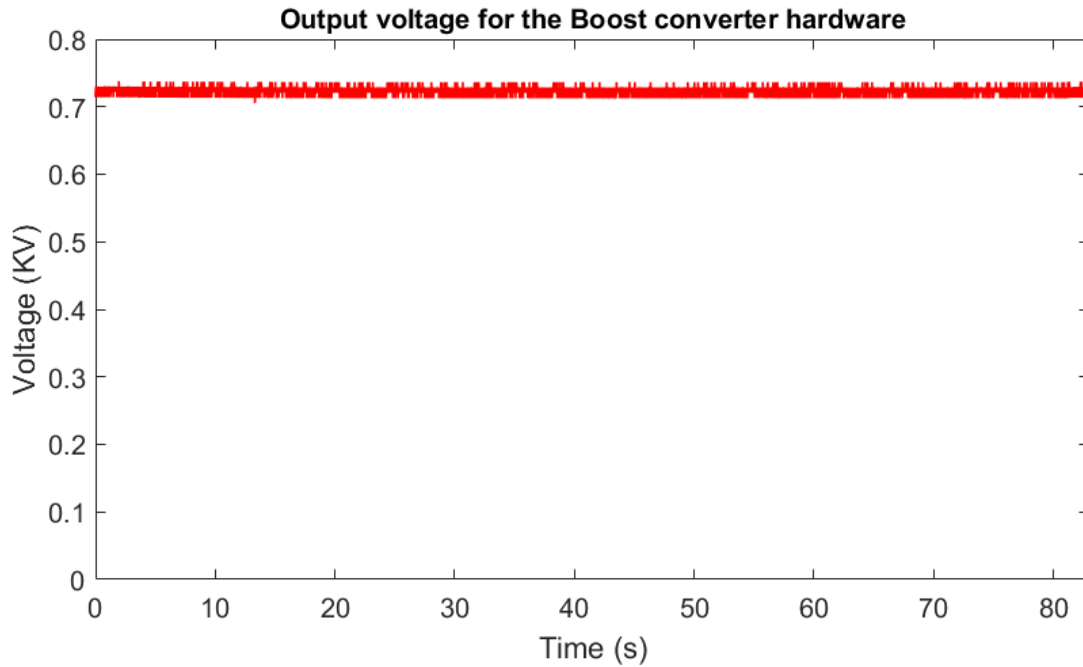


Figure 4.9: Output Voltage of the Boost Converter Hardware during MPPT operation

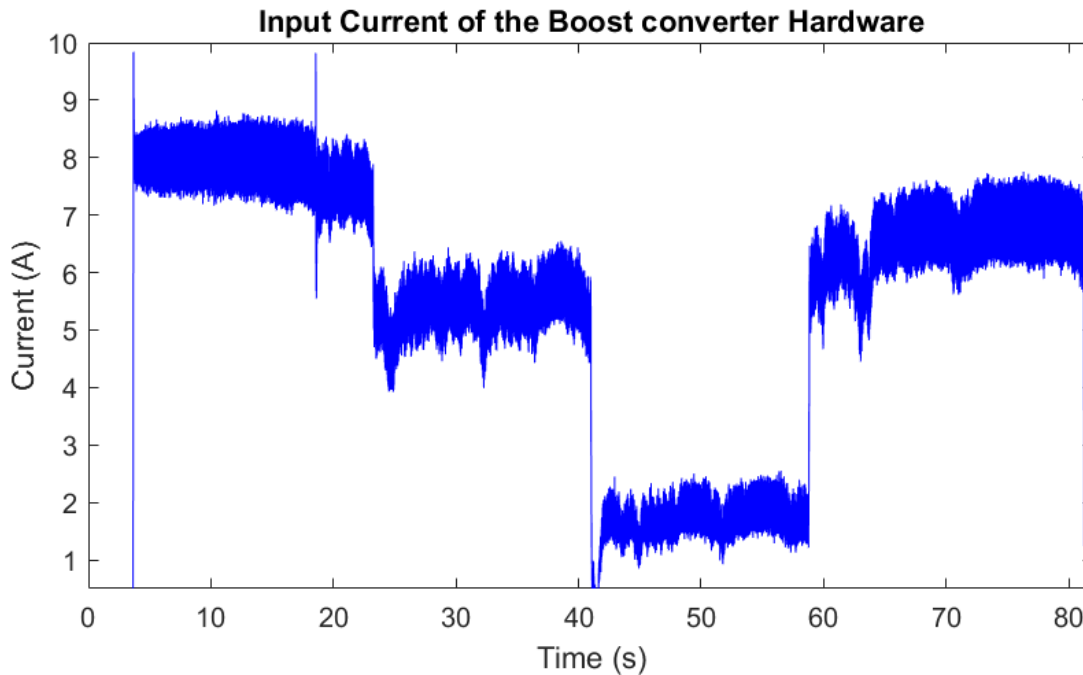


Figure 4.10: Input Current of the Boost Converter Hardware during MPPT

The waveform shown in Figure 4.10 represents the behaviour of the input current under different irradiance values. As the irradiance drop from  $G = 1000W/m^2$  to  $G = 200W/m^2$ , the current drops

and when it is increased to  $G = 700W/m^2$ , it rises.



Figure 4.11: MPP Point tracking on the I-V and P-V Curves for hardware

Figure 4.11 shows the marked operation point of the converter on the I-V and the P-V curves for the MPPT operation of the Boost Converter Hardware.

After the MPPT operation was examined on hardware, the MPPT to Droop control switching was carried out. The hardware results for the same are shown in Figures 4.12, 4.13 and 4.14.

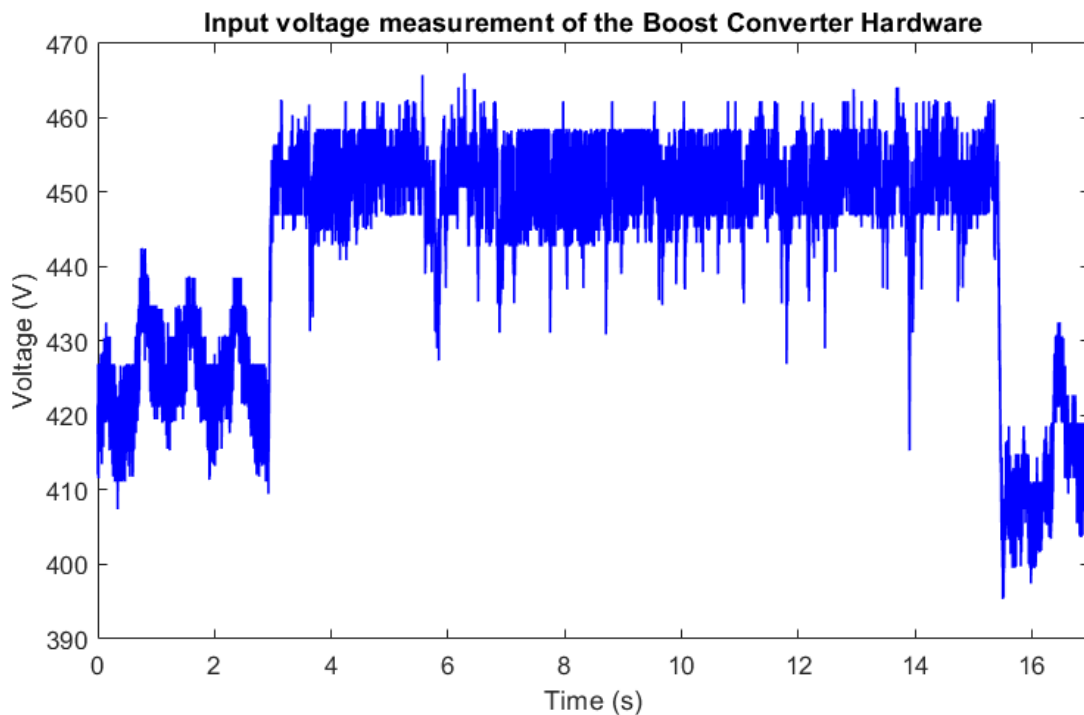


Figure 4.12: Input Voltage of the Boost Converter during MPPT to Droop switching

In order to switch the state from MPPT to Droop operation, the output voltage of the grid was raised from 720V to 750V at 3 seconds as can be observed in Figure 4.13. As a result of that, the input voltage also increased to meet the requirement at the grid.

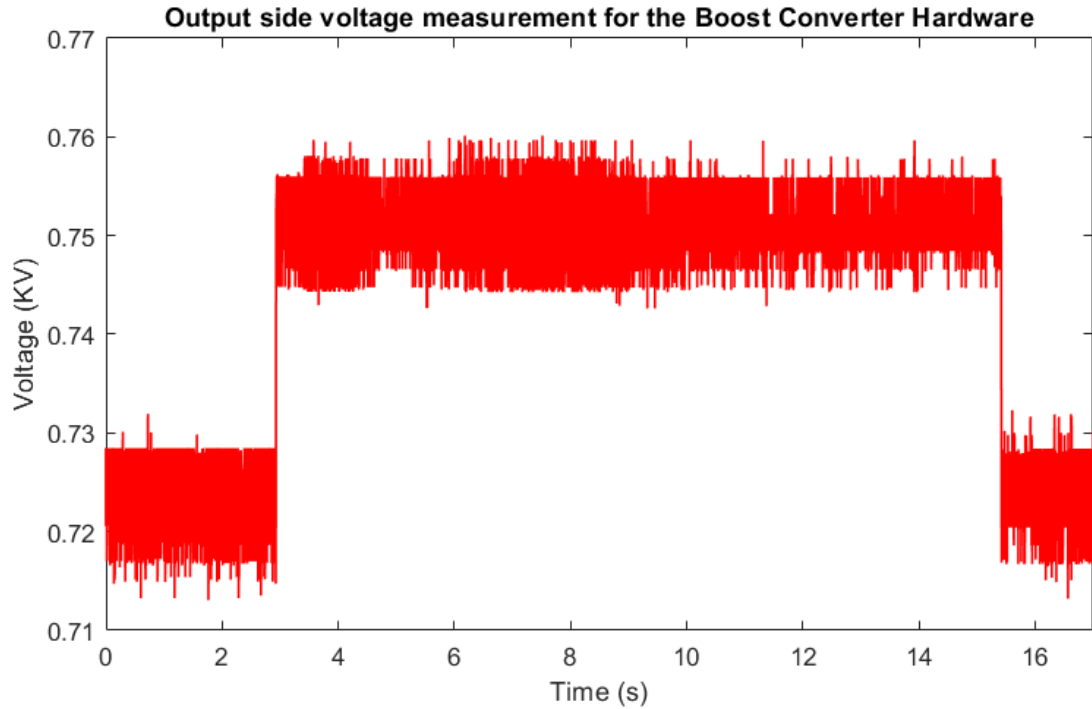


Figure 4.13: Output Voltage of the Boost Converter during MPPT to Droop switching

Since the output side voltage rises, the input current is limited from 4A to 2A as can be seen in Figure 4.14. In this manner the operation of the converter on the droop slope is thus observed and validated according to the implemented strategy.

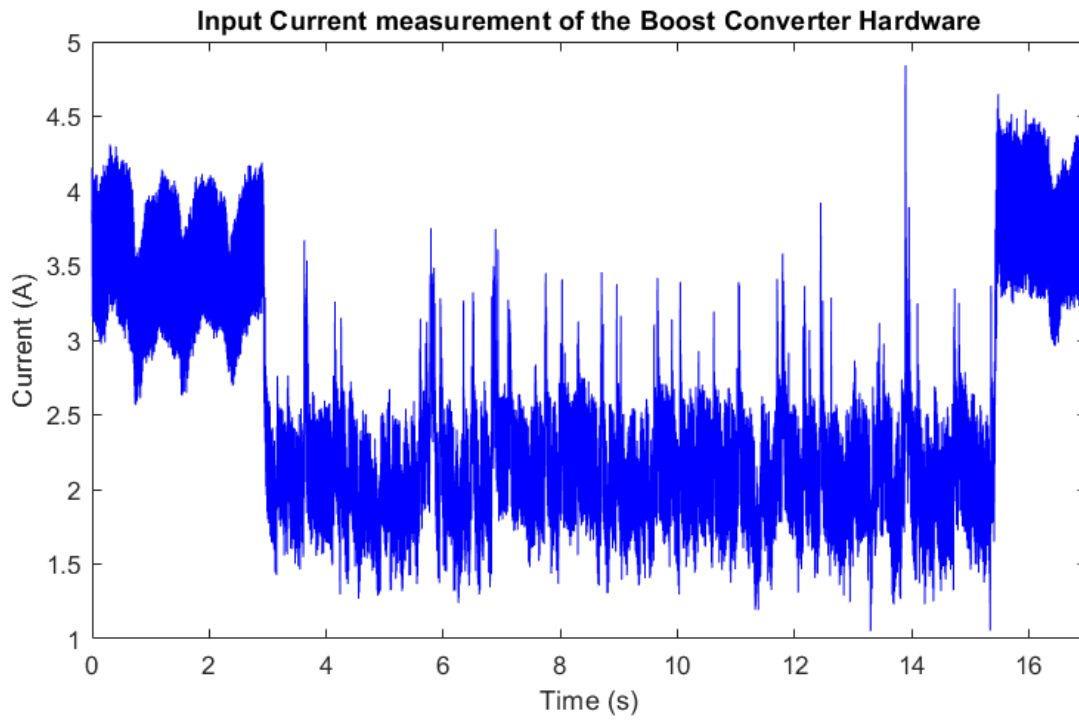


Figure 4.14: Input Current of the Boost Converter during MPPT to Droop switching

At 15.5 seconds, the output voltage is reduced to 720V to switch the state from Droop to MPPT operation. As a result, the input voltage also reduces to approximately 400V and the current increases thus entering the MPPT mode of operation.

## 4.2 MPPT Boost Converter for Bipolar DC Microgrids

### 4.2.1 Hardware Results

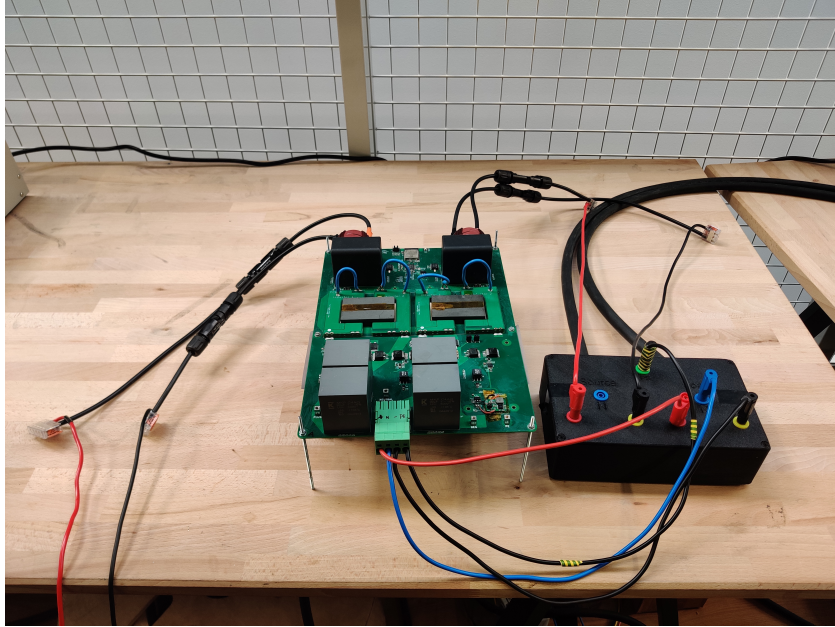


Figure 4.15: Hardware of the MPPT Boost Converter for Bipolar DC Microgrids

The hardware test was started by using one Delta power supply at the input of the negative side of the converter and using the Delta power supply at the output side. The operation was performed for MPPT. The Irradiance was set to approximately  $G = 800W/m^2$  and input was set at approximately  $V_{mpp} = 130V$  and  $I_{mpp} = 5A$  for that irradiance value. the output side i.e. grid voltage at  $V_{out} = -320V$ .

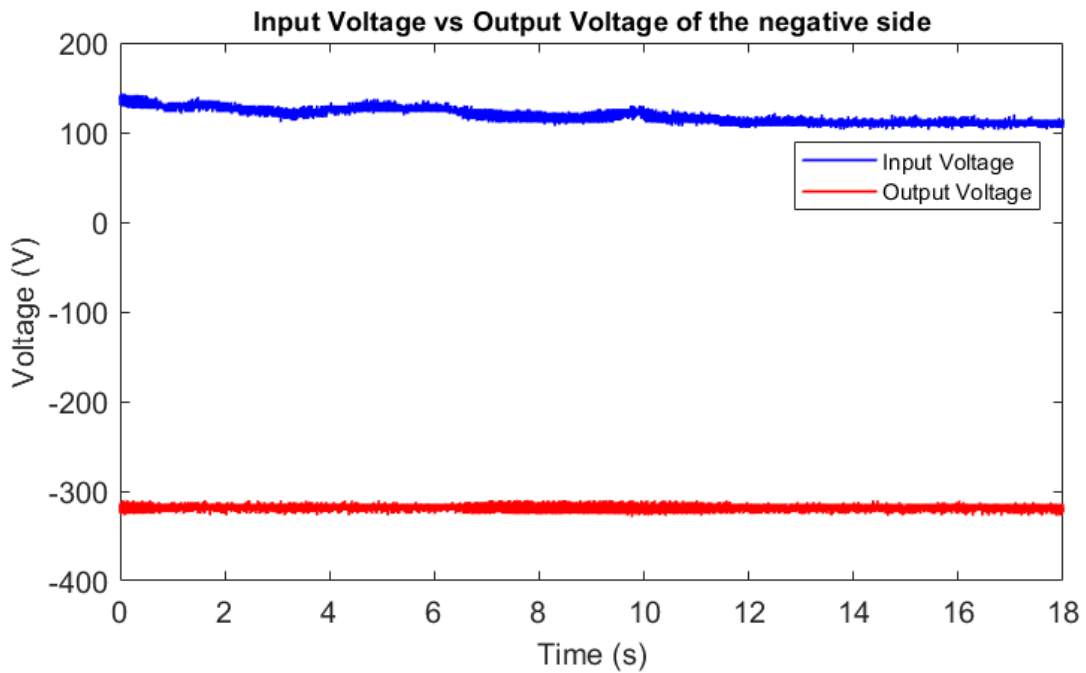


Figure 4.16: MPPT Control test on the Hardware of the negative side

The voltage plot in Figure 4.16 shows the input voltage in blue and the output voltage in red. Since the negative side was powered, the output is at  $V_{out} = -320V$ .

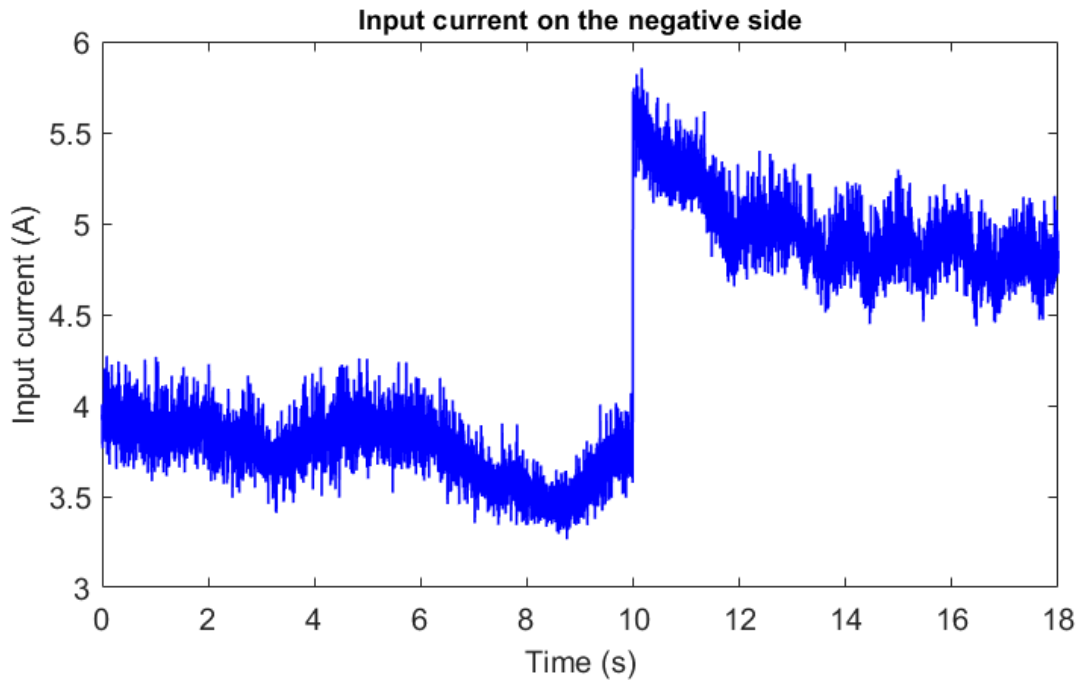


Figure 4.17: Change in input current resulted due to change in Irradiance

As observed in Figure 4.17, when the irradiance is lesser i.e.  $600W/m^2$ , the input current is lesser i.e at 4A. At 10 seconds, the Irradiance was changed to approximately  $G = 800W/m^2$  and as a result, the input current increases to 5A. The change in the input current resulting due to the change in irradiance thus helps in validating the implementation of the MPPT control.

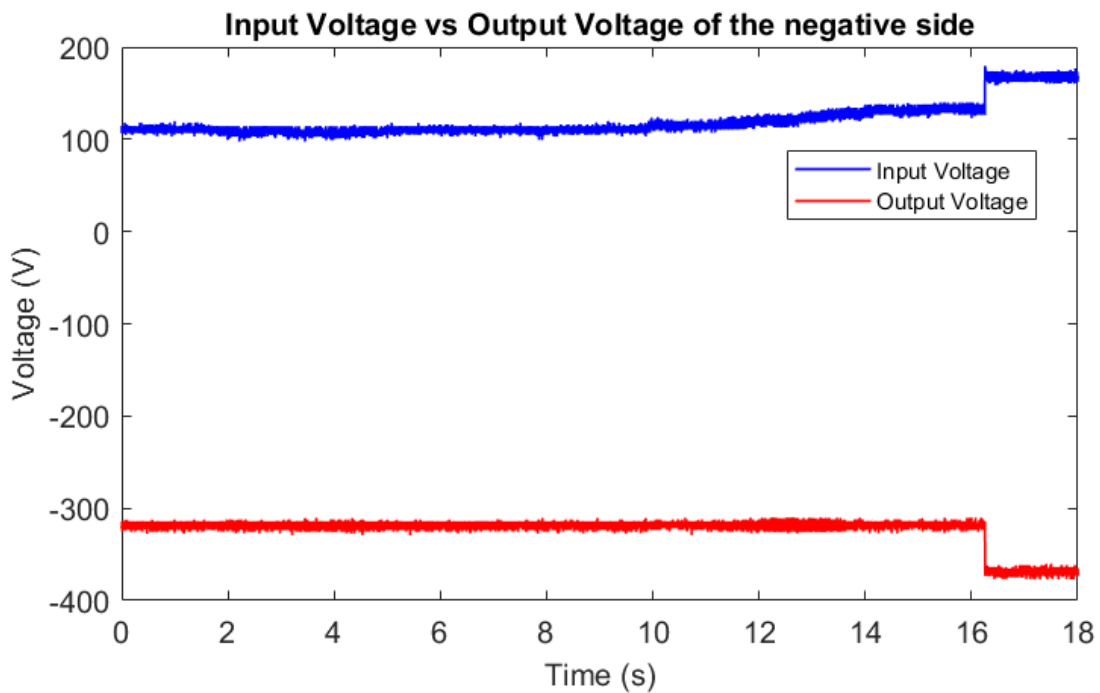


Figure 4.18: MPPT to Droop control switching test

The test was continued while keeping the irradiance constant. At 10 seconds, the irradiance was again changed to  $G = 600W/m^2$  which results into a reduction in the input current as expected. As the current settles around the 4A set point generated, at 16 seconds, the output voltage was increased to  $V_{out} = 370V$ .

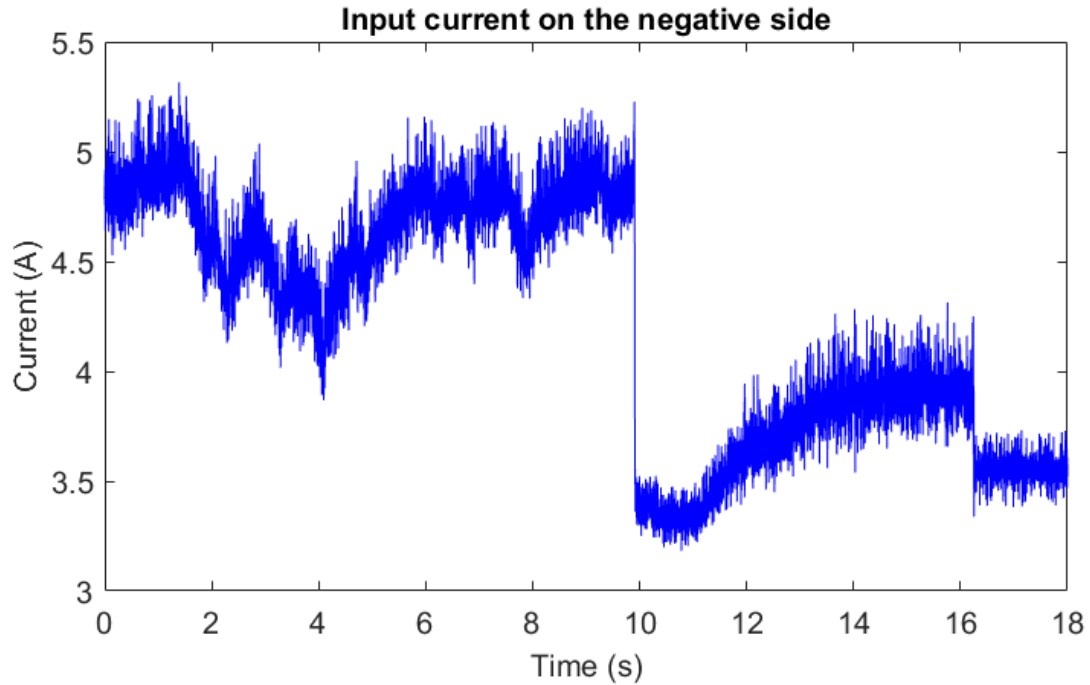


Figure 4.19: Output and Neutral point voltages of the Bipolar

The current reduces as the input voltage rises as observed in Figure 4.19. Between 10 and 16 seconds the current tries to go to the 4A set point. This thus reassures that the MPPT to Droop control switching is successful on the hardware.

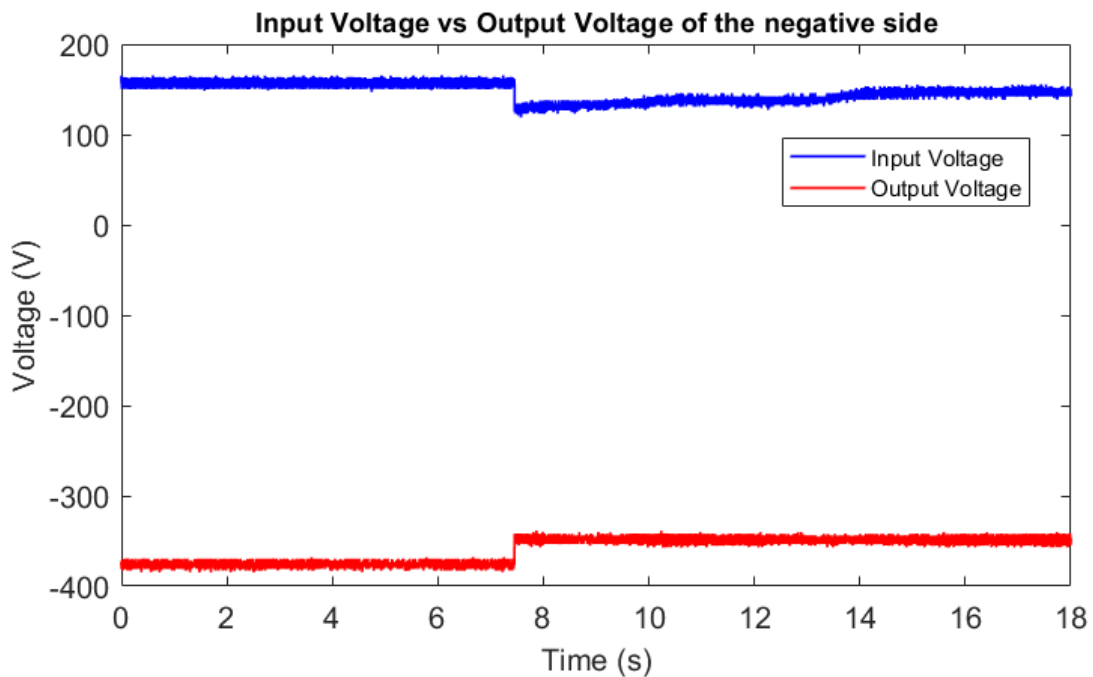


Figure 4.20: MPPT Control test on the Hardware of the negative side

Figure 4.20 shows the continued test in Droop control. The grid voltage at the output side is 375V as seen in Figure 4.20 and the current seen in 4.21 is at 0.2A, and at approximately 8 seconds, the control is switched from Droop to MPPT. The grid voltage is reduced from 375V to 350V. As the voltage is reduced to 350V and as seen, the input current rises quickly to the generated set point of 3.5A. As thus observed, the switching from Droop control back to MPPT control is successfully achieved.

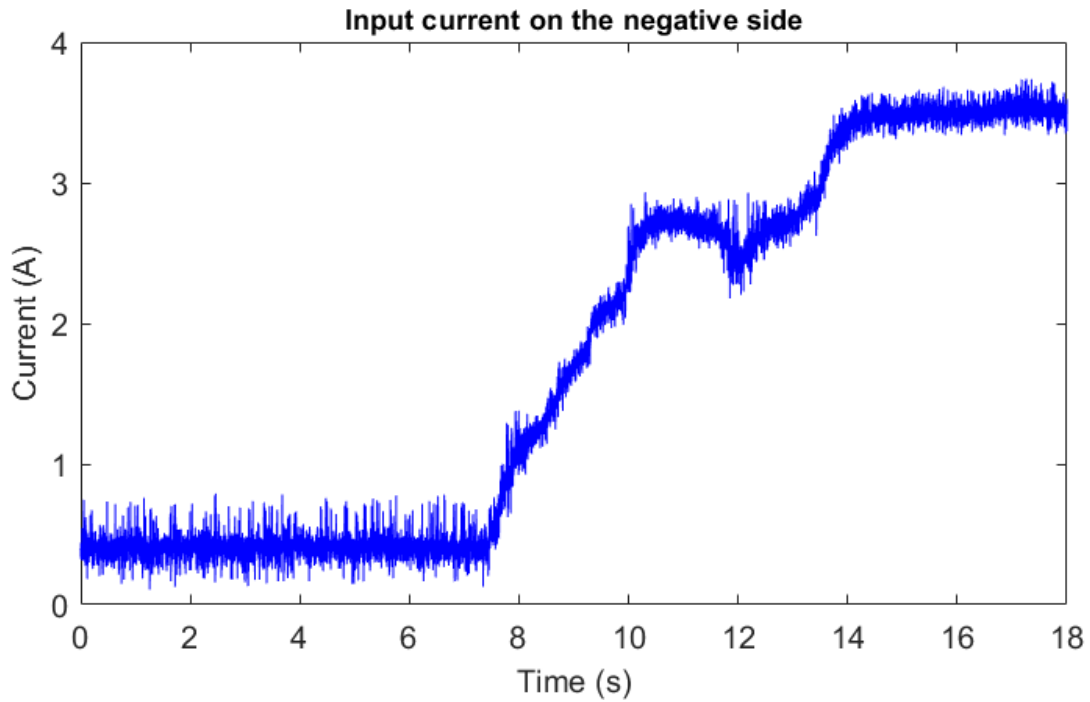


Figure 4.21: Change in input current resulted due to change in Irradiance

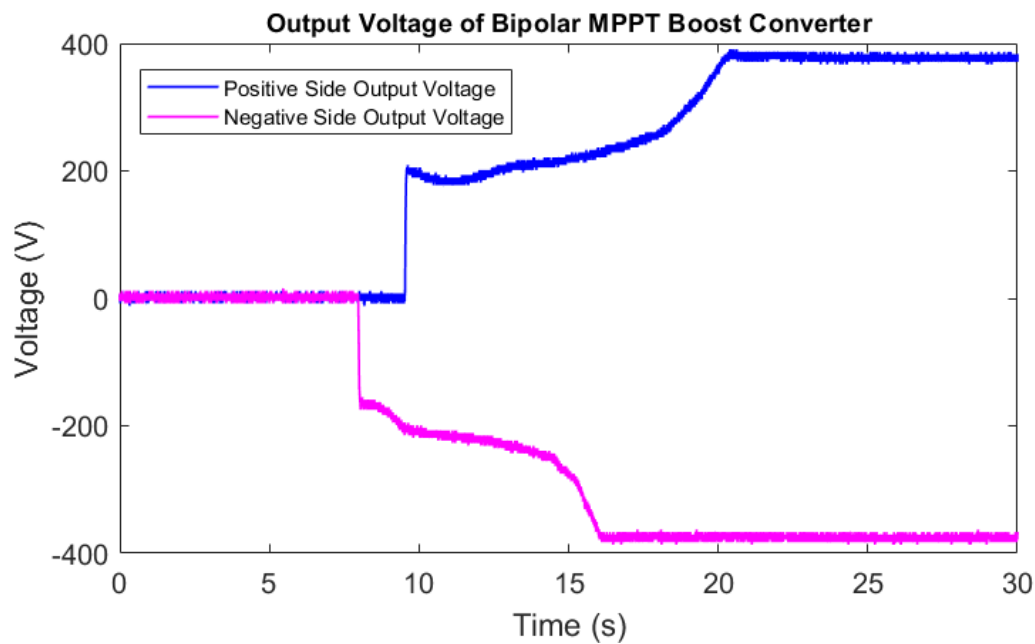


Figure 4.22: Output and Neutral point voltages of the Bipolar

Figure 4.22 shows the output voltage measurements for the MPPT Boost converter for the Bipolar

DC Microgrid. Here both, the positive and the negative side of the converter are powered. The input side between the positive and the neutral point was a PV simulator with an input voltage of  $V_{in,P} = 200V$  which is boosted to approximately  $V_{out,P} = 380V$ . Similarly, the PV simulator between the neutral point and the negative side input the PV simulator with an input voltage of  $V_{in,N} = 200V$  which is boosted to approximately  $V_{out,N} = 380V$ . The operation was performed in MPPT mode. The simulations and the testing procedures did help in extraction of helpful information related to the control designed for these converter topologies. It can be indicated that the control designed based on the model of the converters, functions on the hardware. When the irradiance is varied, the input current is also affected without causing any instability for the operational conditions described. The P&O MPPT algorithm gives expected output with respect to variations in the operating conditions. When there is a requirement to switch the state between MPPT and Droop operation, the state machine responds as it should and thus the operation in both, MPPT and Droop states is thus possible.

## 5.1 Conclusion

This section elaborates on the discussion on the answers of the research questions.

### 5.1.1 Discussion on the research questions

This subsection focuses on the manner this thesis answers the research questions.

- **How does the PV model made affect the control of the MPPT Converter?**

The model of the PV generator has been made for the MPP operation point by linearization. This model helps in order to evaluate the performance of the cascaded PI controller under maximum power point operating condition. In addition this model can be used for different operating points to track the performance of the cascaded PI controller.

- **How can MPPT converters be operated in islanded and grid connected modes of operation?**

By implementing Droop control, the converter can make a transition from MPPT operation to Droop operation during islanded operation. In islanded mode of operation, if the DC microgrid does not require the amount of power generated by the converter, then the Droop mode of operation is activated since the MPP operation is not required due to lesser power demand. In this manner, the power balance is maintained to avoid any over-voltage at the grid side.

## 5.2 Further Developments

In this thesis, the hardware implementation has been done with a DC source which emulates the grid. And it would be interesting to observe the real time implementation of this control with an actual DC Microgrid since it will bring more challenges due to the dynamics of the DC Microgrid. An improved model of the PV string at the input considering the effect of temperature will also be a nice addition in order to observe its effect on the existing controller.

- [1] DNV. “Solar pv powering through to 2030.” (2019), [Online]. Available: <https://www.dnv.com/to2030/technology/solar-pv-powering-through-to-2030.html> (visited on 2019).
- [2] IRENA. “Global energy transformation.” (2018), [Online]. Available: [https://www.irena.org/-/media/Files/IRENA/Agency/Publication/2018/Apr/IRENA\\_Report\\_GET\\_2018.pdf](https://www.irena.org/-/media/Files/IRENA/Agency/Publication/2018/Apr/IRENA_Report_GET_2018.pdf) (visited on 2018).
- [3] IEA. “World energy outlook 2021, iea, paris.” (2021), [Online]. Available: <https://www.iea.org/reports/world-energy-outlook-2021> (visited on 2021).
- [4] D. J. Hammerstrom, “Ac versus dc distribution systems did we get it right?” In *2007 IEEE Power Engineering Society General Meeting*, 2007, pp. 1–5. DOI: [10.1109/PES.2007.386130](https://doi.org/10.1109/PES.2007.386130).
- [5] A. Stippich, A. Sewergin, G. Engelmann, *et al.*, “From ac to dc: Benefits in household appliances,” in *International ETG Congress 2017*, 2017, pp. 1–6.
- [6] kudzai simau, “Chapter 2 mathematical models of control systems 2.1 introduction 2.2 time-domain mathematical models of control systems 2.2.1 differential equations of linear components and linear systems,”
- [7] V. Ignatenko, A. Yuditsev, and D. Lyapunov, “Application of state-space method for control system analysis,” in *2019 International Siberian Conference on Control and Communications (SIBCON)*, 2019, pp. 1–5. DOI: [10.1109/SIBCON.2019.8729658](https://doi.org/10.1109/SIBCON.2019.8729658).
- [8] P. J. Fernando Silva and P. Sónia Ferreira Pinto, “Control methods for switching power converters,” in *Instituto Superior Técnico, DEEC, CAUTL, Laboratório Máquinas Eléctricas e Electrónica de Potência, AC Energia*, Technical University of Lisbon, Av. Rovisco Pais 1, 1049-001 Lisboa, Portugal, pp. 1–6.
- [9] S. M. Sze, Y. Li, and K. K. Ng, *Physics of semiconductor devices*. John wiley & sons, 2021.
- [10] W. Pfann and W. Van Roosbroeck, “Radioactive and photoelectric p-n junction power sources,” *Journal of Applied Physics*, vol. 25, no. 11, pp. 1422–1434, 1954.
- [11] M. Prince, “Silicon solar energy converters,” *Journal of Applied Physics*, vol. 26, no. 5, pp. 534–540, 1955.
- [12] *Double diode model*. [Online]. Available: <https://www.pveducation.org/pvcdrom/characterisation/double-diode-model>.
- [13] M. Wolf and H. Rauschenbach, “Series resistance effects on solar cell measurements,” *Advanced energy conversion*, vol. 3, no. 2, pp. 455–479, 1963.
- [14] M. G. Villalva, J. R. Gazoli, and E. Ruppert Filho, “Modeling and circuit-based simulation of photovoltaic arrays,” in *2009 Brazilian Power Electronics Conference, IEEE*, 2009, pp. 1244–1254.

- [15] N. Maouhoub, “Analytical identification method for the single diode model parameters of a photovoltaic panel using datasheet values,” *Journal of Nano-and Electronic Physics*, vol. 9, no. 6, 2017.
- [16] J. Cubas, S. Pindado, and C. De Manuel, “Explicit expressions for solar panel equivalent circuit parameters based on analytical formulation and the lambert w-function,” *Energies*, vol. 7, no. 7, pp. 4098–4115, 2014.
- [17] A. H. Smets, K. Jäger, O. Isabella, R. A. Swaaij, and M. Zeman, *Solar Energy: The physics and engineering of photovoltaic conversion, technologies and systems*. UIT Cambridge, 2015.
- [18] “Pv system types and components.” (2020), [Online]. Available: <https://www.e-education.psu.edu/ae868/node/872>.
- [19] E. Planas, J. Andreu, J. I. Gárate, I. M. De Alegria, and E. Ibarra, “Ac and dc technology in microgrids: A review,” *Renewable and Sustainable Energy Reviews*, vol. 43, pp. 726–749, 2015.
- [20] G. R. Panda, and R. Peesapati, “Hardware-in-loop implementation of an adaptive droop control strategy for effective load sharing in dc microgrid,” in *2016 IEEE 6th International Conference on Power Systems (ICPS)*, 2016, pp. 1–6. DOI: [10.1109/ICPES.2016.7584031](https://doi.org/10.1109/ICPES.2016.7584031).
- [21] J. J. Justo, F. Mwasilu, J. Lee, and J.-W. Jung, “Ac-microgrids versus dc-microgrids with distributed energy resources: A review,” *Renewable and sustainable energy reviews*, vol. 24, pp. 387–405, 2013.
- [22] L. Mackay, T. Hailu, L. Ramirez-Elizondo, and P. Bauer, “Towards a dc distribution system—opportunities and challenges,” in *2015 IEEE First International Conference on DC Microgrids (ICDCM)*, IEEE, 2015, pp. 215–220.
- [23] M. Lonkar and S. Ponnaluri, “An overview of dc microgrid operation and control,” in *IREC2015 The Sixth International Renewable Energy Congress*, IEEE, 2015, pp. 1–6.
- [24] S. Sakkas, “Control of a dc microgrid,” 2018.
- [25] S. Dahale, A. Das, N. M. Pindoriya, and S. Rajendran, “An overview of dc-dc converter topologies and controls in dc microgrid,” in *2017 7th International Conference on Power Systems (ICPS)*, 2017, pp. 410–415. DOI: [10.1109/ICPES.2017.8387329](https://doi.org/10.1109/ICPES.2017.8387329).
- [26] N. Mohan, T. M. Undeland, and W. P. Robbins, *Power electronics: converters, applications, and design*. John wiley & sons, 2003.
- [27] S. Verma, S. Singh, and A. Rao, “Overview of control techniques for dc-dc converters,” *Research Journal of Engineering Sciences*, vol. 2, no. 8, pp. 18–21, 2013.
- [28] M. Hlaili and H. Mecherghi, “Comparison of different mppt algorithms with a proposed one using a power estimator for grid connected pv systems,” *International Journal of Photoenergy*, vol. 2016, 2016.
- [29] V. Salas, E. Olias, A. Barrado, and A. Lazaro, “Review of the maximum power point tracking algorithms for stand-alone photovoltaic systems,” *Solar energy materials and solar cells*, vol. 90, no. 11, pp. 1555–1578, 2006.
- [30] R. G. Tapre and R. Deshbhratar, “Comparative study and simulation of different maximum power point tracking (mppt) techniques in a solar power generation,” *International Journal on Recent and Innovation Trends in Computing and Communication*, vol. 3, no. 2, pp. 143–148, 2015.
- [31] S. Luo, Z. Ye, R.-L. Lin, and F. C. Lee, “A classification and evaluation of paralleling methods for power supply modules,” in *30th Annual IEEE Power Electronics Specialists Conference. Record.(Cat. No. 99CH36321)*, IEEE, vol. 2, 1999, pp. 901–908.
- [32] S. Anand, B. G. Fernandes, and J. Guerrero, “Distributed control to ensure proportional load sharing and improve voltage regulation in low-voltage dc microgrids,” *IEEE transactions on power electronics*, vol. 28, no. 4, pp. 1900–1913, 2012.

- [33] Q. Shafiee, T. Dragičević, J. C. Vasquez, and J. M. Guerrero, “Hierarchical control for multiple dc-microgrids clusters,” *IEEE transactions on energy conversion*, vol. 29, no. 4, pp. 922–933, 2014.
- [34] G. Maroulis, *Dc-dc converters for photovoltaic powered dc microgrid*, Jan. 1970. [Online]. Available: <https://repository.tudelft.nl/islandora/object/uuid:78f68bb8-7373-462b-b7af-f65cca545724?collection=education>.